energies

MDPI

Article

Two-Dimensional Gravity Inversion of Basement Relief for Geothermal Energy Potentials at the Harrat Rahat Volcanic Field, Saudi Arabia, Using Particle Swarm Optimization

Faisal Alqahtani [1,2], Ema Michael Abraham [3,*], Essam Aboud [1] and Murad Rajab [1,2]

[1] Geohazards Research Center, King Abdulaziz University, Jeddah 21589, Saudi Arabia; falqahtani@kau.edu.sa (F.A.); eaboudishish@kau.edu.sa (E.A.); mmrajab@kau.edu.sa (M.R.)
[2] Department of Petroleum Geology and Sedimentology, Faculty of Earth Sciences, King Abdulaziz University, Jeddah 21589, Saudi Arabia
[3] Department of Geology/Geophysics, Alex Ekwueme Federal University, Ndufu-Alike Ikwo, P.M.B. 1010, Abakaliki 482131, Ebonyi, Nigeria
* Correspondence: ema.abraham@funai.edu.ng

Abstract: We invert gravity and magnetic anomalies for basement relief at the Harrat Rahat Volcanic Field (HRVF) for the purpose of evaluating its geothermal energy prospects. HRVF is dominated by basaltic scoria cones and other volcanic rocks overlying the Proterozoic basement. The area considered for this study is located within the northern HRVF and consists mainly of alkali basalts with lesser amounts of benmoreite, mugearite, hawaiite, and trachyte. Our approach adopts a global optimization technique using Particle Swarm Optimization with automated parameter selection, and a two-dimensional gravity-magnetic (GM) forward modeling procedure. The results of the PSO-based approach indicate a depth to the basement at 0.10–624 m, with greater depths within the central region of a solitary anomalous density body in the HRVF. The obtained basement geometry is corroborated by the depth estimates obtained from other potential field inversion methods. The regions with higher prospects are mapped for a targeted future geothermal energy exploration at the HRVF, based on our inversion results.

Keywords: geothermal; gravity; inversion; depths; magnetics; reservoir

Citation: Alqahtani, F.; Abraham, E.M.; Aboud, E.; Rajab, M. Two-Dimensional Gravity Inversion of Basement Relief for Geothermal Energy Potentials at the Harrat Rahat Volcanic Field, Saudi Arabia, Using Particle Swarm Optimization. *Energies* **2022**, *15*, 2887. https://doi.org/10.3390/en15082887

Academic Editors: Procesi Monia, Luca Guglielmetti and Jihoon Kim

Received: 5 January 2022
Accepted: 11 April 2022
Published: 14 April 2022

1. Introduction

Geothermal energy is classified as a renewable energy source because heat is continuously produced inside the Earth. Possible applications of this resource are in space heating, industrial usage and electricity generation. In Saudi Arabia, the possible usage of geothermal energy resources is for electric power production. Oil and gas resources currently form the basis for electricity production in Saudi Arabia and a greater percentage of electric power produced is used for cooling purposes [1]. The International Energy Agency, IEA (2012), reported an increase in carbon dioxide (CO_2) emissions in Saudi Arabia from 252,000 Gg to 446,000 Gg, with oil and gas contributing an aggregate of 252,000 Gg. The percent per capita emission of CO_2 increased from 0.012 Gg to 0.016 Gg in the year 2000. This development informed the government's decision to explore and develop alternative and renewable energy sources (e.g., solid waste, solar, geothermal and wind energy sources) to meet the country's energy needs. Lately, there have been renewed interests in crustal structure studies on the Arabian Peninsula [2–5] and within the inner parts of the Arabian lithospheric plate [6–9]. Among the Middle Eastern countries, Saudi Arabia is the most geothermally active [10–13]. Authors [1,10,12–17] have suggested potential geothermal energy areas in Saudi Arabia. More studies to evaluate the geothermal energy potentials of Saudi Arabia are still needed [1,16].

Remote sensing images and two-dimensional electrical resistivity profiles from the Wadi Al-Lith area (Ain Al Harrah) of Saudi Arabia were analyzed with the aim of delineating the surface geological lineaments and subsurface structural elements controlling the main hot spring in the area [18]. The subsurface temperature was found to be 136 °C; the heat flow and discharge enthalpy were 183 mW/m^2 and 219 kj/kg, respectively. The total stored heat energy was also evaluated as 1.713×10^{17} J for rock and fluid and a geothermal reserve potential of 26.99 MWt. A medium-scale power plant was recommended for this location to exploit the available geothermal energy resources.

The geothermal energy potential of the Jizan area, southwest of Saudi Arabia, was analyzed using Landsat and spot satellite images and measurements from a geothermometer [19]. Three main thermal anomalies were recognized (Al Ardah, Al Khouba, and Bani Malik), which originate from hard crystalline rocks. Different water samples collected from the hot springs and water wells in the region were analyzed to determine the subsurface formation temperature, heat flow and water type. Their results show maximum values of up to 152 °C for the subsurface temperatures and 210 mW/m^2 for heat flow in the area. A case study of the Al Khouba area of Jizan, southwestern Saudi Arabia, was conducted using a Landsat satellite image, geothermometer and two-dimensional electrical resistivity survey [16]. The significant presence of geothermal anomalies was realized in the province with appreciable petrothermal properties reaching 78 °C. The estimated thermal parameters were the heat flow $(144\ mW/m^2)$, discharge enthalpy $(318\ kj/kg)$ and subsurface temperature $(133\ °C)$, respectively. They estimated the geothermal potential at 17.847 MWt for the Al-Khouba hot spring, with a reservoir area of 1.125 km^3. A further scientific investigation was strongly recommended.

A study on the Ayn Al-Wagara hot spring in the Jizan province [20] using hydrochemical and electrical resistivity data showed thermal water reaching a temperature of 116 °C within the zone. Data from 730 gravity stations, 170 Audio Magnetotelluric (AMT) stations and aeromagnetic surveys were analyzed for the geothermal potential of the Khayber volcanic field [21]. Two zones with a high geothermal energy potential were identified, and slim hole drilling was recommended. Future gravity and magnetotelluric surveys were recommended on the Harrat Khayber and Harrat Rahat Volcanic Field (HRVF) by Berthier et al. [20]. They concluded that, from the analysis of the volcanology and geochemical data, a shallow geothermal reservoir may exist in the Cambrian sandstone of Harrat Khayber, whereas a significant self-sealing existed at the top of the geothermal reservoir at Harrat Rahat, resulting in the lack of hydrothermal manifestations in the region.

Al-Douri et al. [22] examined the geothermal energy reserve and potential at the eastern region of Saudi Arabia, in the Ain Al Harrah region. They analyzed reports and studies to conclude that the region held adequate geothermal potentials and subsequently recommended the region for the direct investment of the geothermal energy infrastructure. Previously, Rehman [12] drew attention to the existing, ongoing and planned sources of geothermal energy in Saudi Arabia, and recommended quantitative and qualitative explorations of these sources. Other geoscientific studies conducted in the northern region of the HRVF for various probes include crustal imaging for magma intrusions using seismic techniques [23,24] and magnetotellurics (MT) [25], the appraisal of lava morphotypes [26], and the examination of the thickness of lava flows and subsurface structures from gravity and/or aeromagnetic data [27–29]. The seismic studies made various conclusions, ranging from suggesting the possible existence and nonexistence of magma chambers within the region. The lava examinations suggested the recovery of insights into its emplacement mechanism through the morphotypes. The magnetic and gravity results indicate various basement depths, including lava thickness (~100 m a.s.l.) at the eastern borders [28], and extending deeper to about 600 m at some regions [27,28] and >1000 m [28] at others. The MT examination suggested the presence of 4 major resistivity structures with varying depths reaching 18 km.

For our geothermal energy potential study, we restricted our focus to an area (longitudes 39°40′–39°52′ E and latitudes 24°9′–24°20′ N) identified by these previous studies as possessive of very thick lava flows, located within the center of the HRVF and underneath the historical eruption of 1256 A.D. This location is presumed to support the existence of a basin under the volcanic field with promising potential for exploiting geothermal energy resources. The inversion of the basement relief for known density distributions possesses special significance in numerous practical implementations, such as geothermal and mineral explorations [30]. A mathematical process of attempting to optimize the parameters of a starting model to arrive at a good match to the observed data constitutes the interpretation of gravity data [31]. The problem of ambiguity associated with gravity data interpretation is handled by assigning a mathematical geometry to the anomaly-causing body using a familiar density contrast [31,32]. In other words, one parameter is fixed and the other is estimated using a suitable optimization technique. Some authors [30,33–38] developed 2D/2.5D local optimization techniques over 2D/2.5D sedimentary basins to interpret the gravity anomalies with a constant density function. An attempt was made to invert the gravity data acquired over the sedimentary cover–metamorphic basement of the Aegean Graben System, western Anatolia, Turkey, using a differential evolution algorithm [39]. They showed shallow depths to the metamorphic basement in the grabens, which is contrary to the conclusions obtained from previous studies. Other studies include using a fast inversion of basement reliefs, with an extended Gauss–Newton optimization technique [40], the Levenberg–Marquardt algorithm for gravity inversion [41], nonlinear conjugate gradient for combined gravity and gravity inversion [42] and a combination of normalized vertical derivatives and multi-norm with nonlinear conjugate gradient for the three-dimensional gravity basement relief [43]. Considering the global optimization algorithms, the genetic algorithm for two-dimensional and three-dimensional gravity inversions [44], a very fast simulated annealing method is required for residual gravity inversion [45] and Particle Swarm Optimization (PSO) for fault structure optimization from the gravity data [46,47]. PSO is a robust stochastic optimization technique and one of the most popular global optimization algorithms, due to its minimum control parameter requirement and simple implementation. Depending on the model conceptualization, the inversion of the basement relief in sedimentary basins from gravity data can be suggested as a two-dimensional or three-dimensional problem. The two-dimensional case consists of the inversion of one or different profiles across the basin, generally containing its maximum depth. When the basin is elongated, a common approach consists of inverting several profiles that are orthogonal to its longest dimension, which, analyzed together, serve to depict a pseudo-three-dimensional model. A full family of PSOs is applied to the gravity data for a two-dimensional basement inversion and uncertainty assessment of the basement relief in sedimentary basins [48,49] and three-dimensional models [50]. The application of their algorithm to synthetic and real cases indicate the possibility of performing a fast inversion, together with the assessment of the gravimetric model uncertainty from the sampling, while optimizing the routine. For the present study, we endeavor to invert the recently acquired ground gravity data at the HRVF to determine the basement topography of the region using the PSO technique. This study utilizes a Fourier domain depth profile representation and optimization with PSOs for the depth varying density contrast recently proposed by Roy et al. [30] to appraise the depths to the basement at the HRVF.

Geological Setting

Potential geothermal reservoirs may exist in the volcano-detrital series, which forms the substratum of Harrat Rahat [10]. The structural complexity of the crust can be described using five seismic layers in the eastern region and three layers in the western region of the Arabian Plate [8]. A crystalline basement of the Precambrian continental crust constitutes the plate and is about 40–45 km thick with an age of 870–550 Ma. The composition also includes a layered succession of younger Phanerozoic sedimentary rocks with an age varying from the Cambrian (540 Ma) to Pleistocene Ages, having a thickness of 0–10 km, surficial

Cenozoic flood basalt, and intracontinental Paleogene–Holocene with present oceanic basins in the direction of the Red Sea and the Gulf of Aden [12]. Harrat Khaybar and Harrat Rahat are notable volcanic fields covering larger parts of the western Arabian Plate and have been noted [14,20] to retain high prospects for geothermal energy. Harrat Rahat is situated to the east of the Red Sea, on the western margin of the Arabian Peninsula (Figure 1).

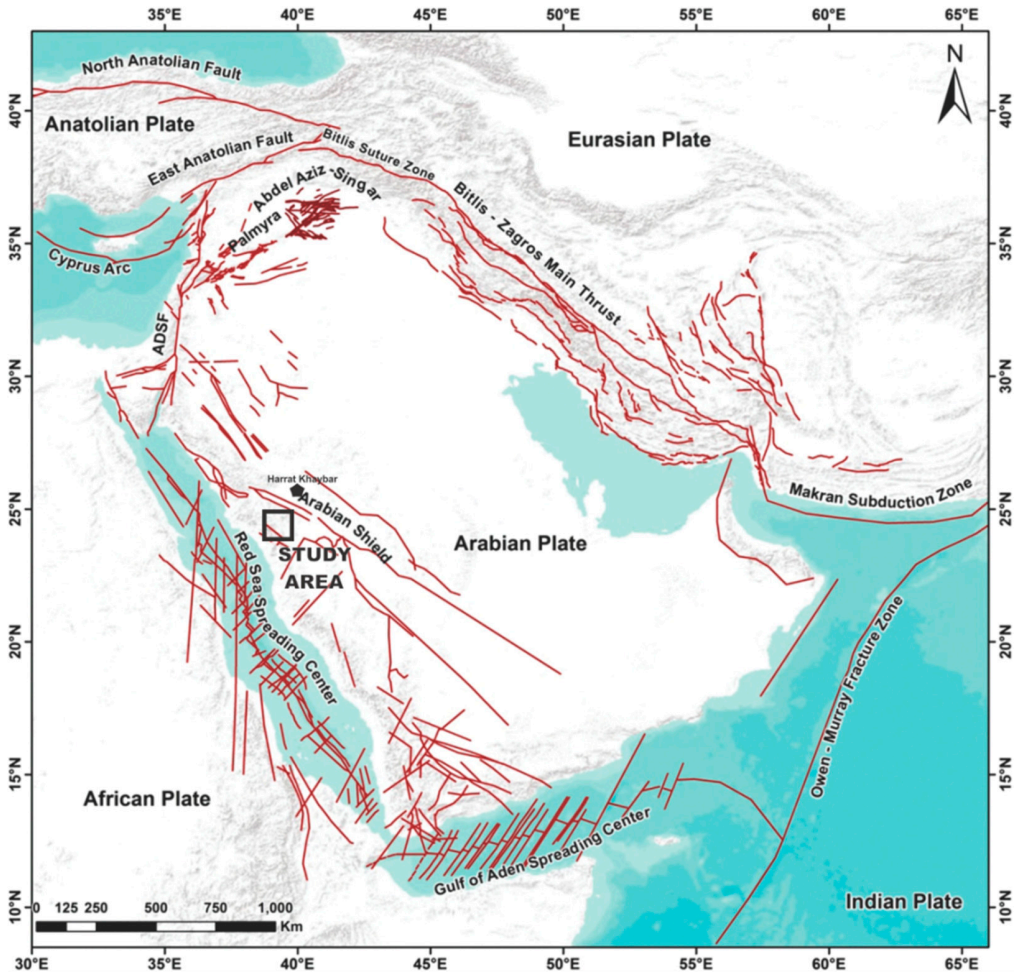

Figure 1. A map display of the Arabian Plate with its tectonic components (modified from [2]). The study area is indicated by the inserted black square.

It is one of the largest volcanic fields on the western margin of the peninsula and a part of the Red Sea rift. At an approximate coverage area of 20,000 km^2, the Harrat Rahat evolution commenced at 10 Ma [51] with 24 domes, 644 scoria cones, and 36 shield volcanoes [12]. Within the region, 32 geologic units that erupted within the northern HRVF after 1 Ma were recently investigated and mapped [52]. These units are composed of intraplate alkali, continental and tholeiitic basalts, hawaiites, as well as mugearite. The volcanic eruption that occurred in 1256 A.D. remains the most recent in this area. A 2.25 km long fissure eruption (Al-Madinah eruption) produced a lava flow as long as 23 km east of Medina [23,52,53]. The eruption that occurred in 1256 A.D. lasted for 52 days, extruded 0.5 km^3 of alkali-olivine basalt (Figure 2) from a 2.25 km long fissure and produced 6scoria cones. This 23 km long lava flow extended to almost 8 km from the city of Al-Madinah [28,53,54].

A variety of extruded basaltic rocks includes alkaline olivine basalts to hawaiite, as well as olivine transitional basalts. Benmoreite, mugerarite, and trachyte basically exist as tuff and dome cones, including lava flows [56,57]. The Harrat Al-Madinah basalts were additionally segmented into lower and upper Al-Madinah Al-Munawwarah basalts [51,53,55]. Three flow units (Figure 2) constitute the upper Al-Madinah Al-Munawwarah basalts, namely Qm1

(~1.7–1.2 Ma), Qm2 (~1.2–0.9 Ma), and Qm3 (~0.9–0.6 Ma), whereas four flow units, Qm4 (~0.6–0.3 Ma), Qm5 (~0.3 Ma–4500 BP), and Qm6 (~4500–1500 BP), constitute the upper Al-Madinah Al-Munawwarah basalts [28,51,53,55]. The Cenozoic volcanic rocks of the region lap onto and overlie the Proterozoic rocks, which are comprised of volcanic arc rocks and younger volcanic sedimentary successions. Previously, Berthier et al. [20] observed the indication of a structure running transverse to the general alignment of Harrat Khaybar, which acted as a trap for differentiated magmatic products since the Upper Pleistocene, therefore rendering the Harrat Rahat zone particularly favorable for the presence of an abnormal heat flow. They suggested the area for a high-enthalpy geothermal source presence. A hot magmatic intrusion may exist at depths within this area, thereby implying a higher geothermal energy potential. Ambient noise cross-correlation analysis was applied to the areas of the Harrat Rahat (Figure 3) to investigate the geothermal potentials and high heat flow [1]. This method uses the seismic noise background to infer the crustal velocity structure [58,59], and has recently been applied to geothermal areas and other regions with ahigh heat flow [1,60,61]. The area with a blue coloration in the inserted yellow square of Figure 4 denotes an area of likely high subsurface heat flow based on the young volcanics as mapped from the surface geology [1].

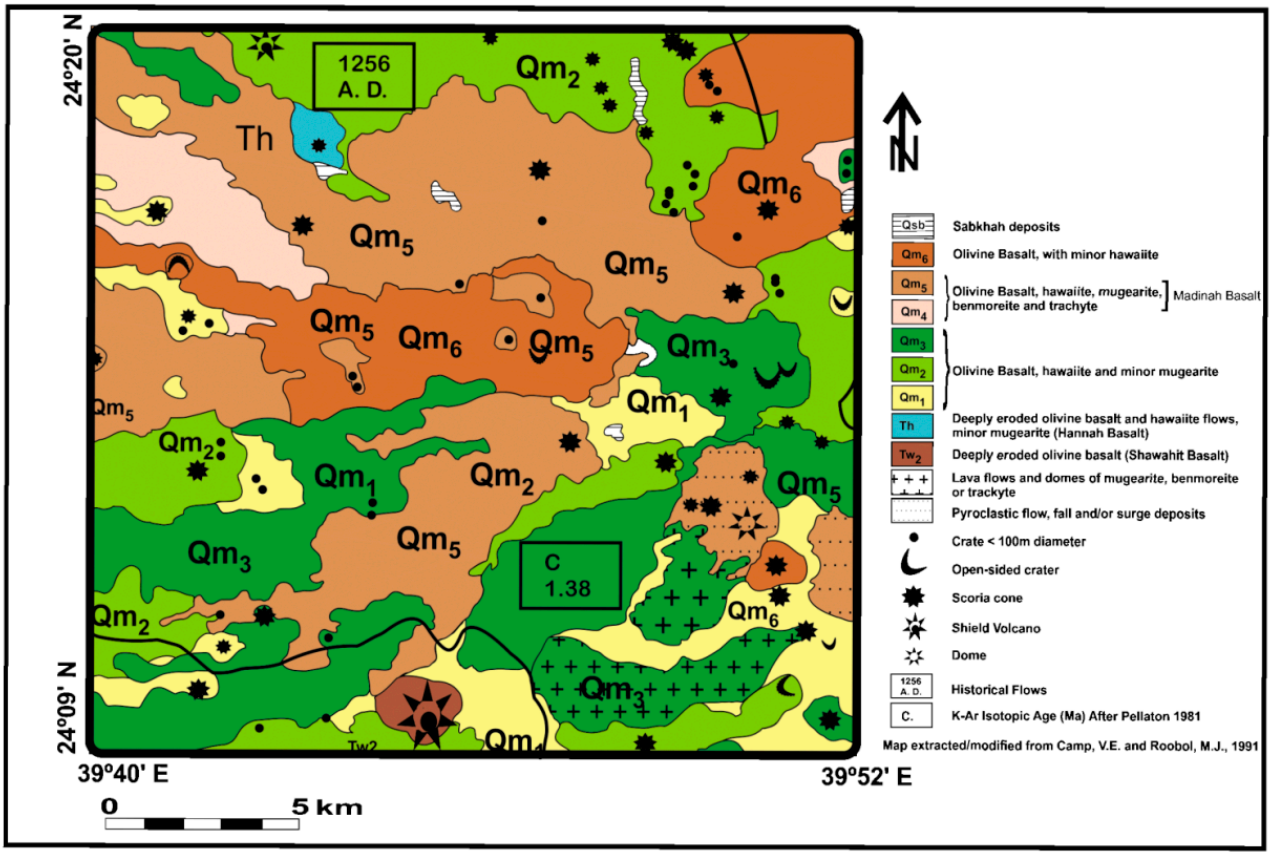

Figure 2. The geologic setting of the study area, part of the northern HRVF (modified after [55]).

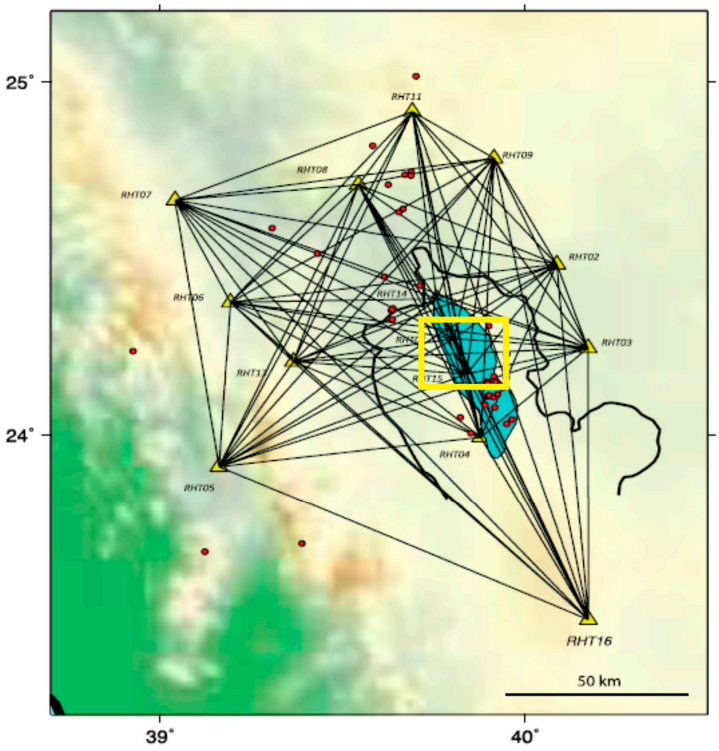

Figure 3. The ray paths covered by the ambient noise correlation showing seismic stations (RHTs) and the outline of northern Harrat Rahat. The blue area denotes an area of a likely high subsurface heat flow based on the young volcanics as mapped from the surface geology. Velocity models have been generated for each path (modified from [1]).

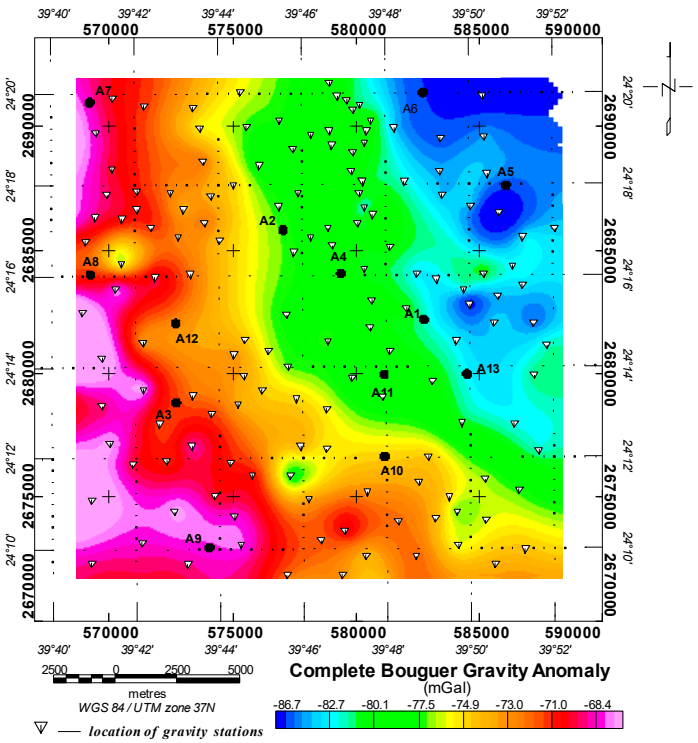

Figure 4. The complete Bouguer gravity anomaly map of the study region. The inverted white triangles, symbolize the gravity measurement stations within the study area. The "A" labels with accompanying numbers represent the Al–Madinah Al–Munawwarah region. The numbers used here designate the various locations within the Al–Madinah Al–Munawwarah region.

2. Materials and Methods

2.1. Data Acquisition and Processing

The study area covers approximately 493 km^2 and adequate efforts were made to collect the gravity data, with reasonable spacing between the measurement points. The gravity survey took place in October 2021 using the Scintrex Autograv CG5 gravity meter. About 149 gravity measurements were performed at the field, with an approximate spacing of 0.2–1 km within the study area (Figure 4). The location of each gravity measurement station was guided by the GPS and visualized using the Global Mapper™ software. The elevations of the gravity measurements sites were obtained using GPS. The gravity measurements were corrected for the tidal variations, instrument drifts over time, and, subsequently, tied to the absolute gravity station AG0191 situated at the Madinah Technical College campus (978,710.191 mGal, 24°28′52″ N, 39°42′56″ E, height (elevation) = 673 m).

Geosoft Oasis Montaj™ software scripts were utilized to compute the free-air and Bouguer gravity anomalies (BGAs) with the respective data uncertainties. The BGA was computed according to the following correction formula:

$$BGA = FAA - 0.0419088.[\rho.Z_s + (\rho_w - \rho) + \rho_w] \quad (1)$$

where the BGA is the Bouguer gravity anomaly (mGal), FAA is the free-air anomaly (mGal), ρ is the reduction density $\left(kg/m^3\right)$, Z_s is the station elevation (m), and ρ_w is the water density, set to 1000 kg/m^3. In the inner zone, the terrain correction was calculated by the software for each point using the flat-topped square prism approach [62]. In the far zone, the terrain correction was based on the annular ring segment approximation to a square prism [63]. The algorithm sums up the effects of four tilted triangular sections, which describe a surface between the gravity station and the elevation at each diagonal corner. A standard crustal reduction density of 2670 kg/m^3 was used. The calculated BGA is estimated to be accurate to <0.12 mGal, with the majority of the values accurate to <0.0269 mGal, and presented in Figure 4. The regional-residual separation is usually accomplished by using polynomial trend surfaces, wavelength filtering, upward continuation, and minimum curvature techniques [64–67]. For this study, a sensitivity examination was adopted, where the first-, second-, and third-order trends were independently removed from the BGA using the polynomial approximation method to examine the best residual outputs that possibly represent the gravity effect of the main geologic features of geothermal interest. In this method, the regional and residual fields are represented by low and high order surfaces, respectively. The third-order trend removal of the regional gravity effect, using least square fitting to all the values in the grid, produceda reliable residual anomaly map (Figure 5), which was subsequently used for further analysis in the present study. The configuration of the gravity anomalies in Harrat Rahat does not change appreciably when using lower crustal reduction densities (2670 kg/m^3), as might be expected fora topography composed of low-density volcanic rocks. This is because the Harrat volcanic field has generally subdued topography [27].

To understand if the boundaries between the various lava flows are reflected in the gravity anomalies, we superimposed a contour plot of Figure 5 onto Figure 2 (Figure 5).

Observed sources of the residual gravity lows lies mainly below the Olivine basalt, Hawaiite, Mugearite and Benmoreite basalts (Figure 6) at the central region of the study area. Taking advantage of a joint inversion procedure for a more reliable and constrained result, we introduced aeromagnetic data into the modeling scheme. A collection of the aeromagnetic datasets, collected variously from 1962 to 1983, with approval from the Ministry of Petroleum and Mineral Resources of the Kingdom of Saudi Arabia, was used for the present study. Surveys were conducted over assigned individual blocks with ground clearances of 150, 300, and 500 m, using a line spacing of about 800 m. The International Geomagnetic Reference Field was subtracted from the total field measurements to obtain the total-field anomalies. The aeromagnetic anomalies in Figure 7 were reduced to pole, as discussed by Zahran et al. [21].

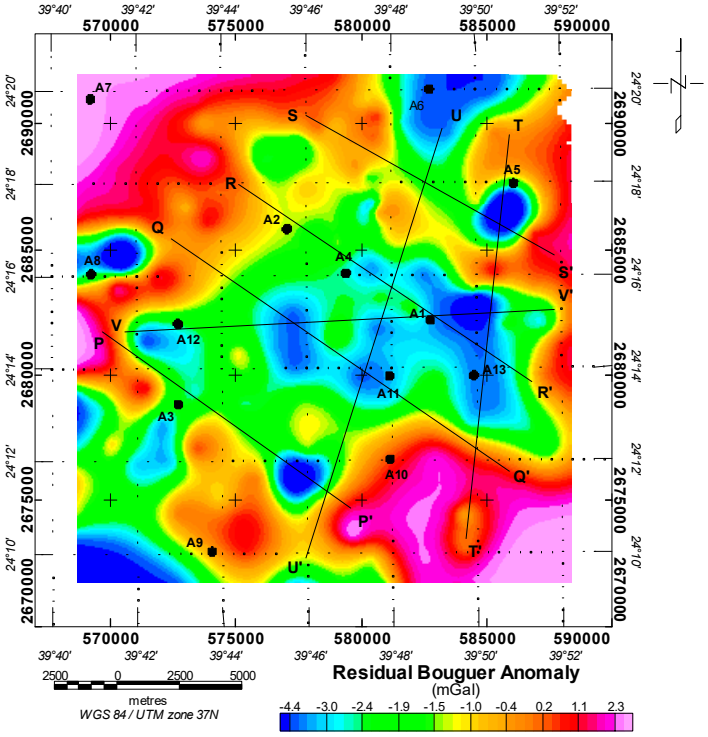

Figure 5. The residual Bouguer anomaly map of the study region. A unique negative gravity anomaly feature can be identified in the central region of the map, with negative gravity anomalies in the northeast (A5 and A6). Similar anomalies can also be observed in the western (A1 and A13) and central (A11) regions. The profiles taken across the identified anomalous region (Profiles PP′, QQ′, RR′, SS′, TT′, UU′, and VV′) are used for the modeling procedures in this study.

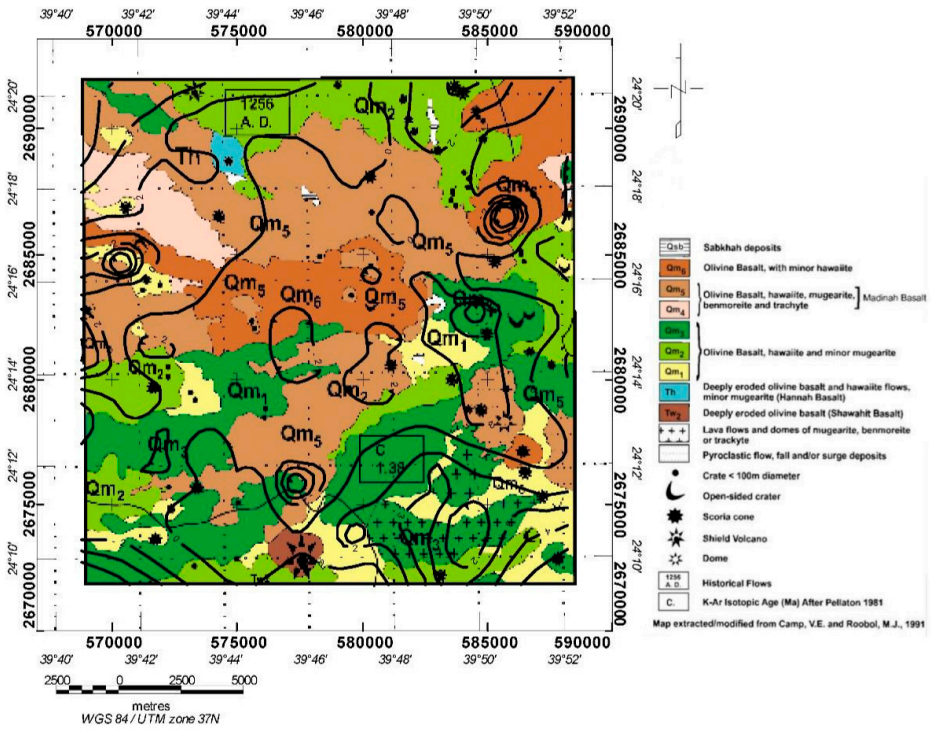

Figure 6. The residual gravity anomalies are superimposed on the surface geology map of the study area. A unique anomaly feature with negative gravity lows recognized in Figure 5 is traced to the geologic region with olivine basalts (Qm1, Qm3, Qm5, and Qm6) within the central part of the study area. The existence of this anomaly feature makes this region desirable for further evaluations.

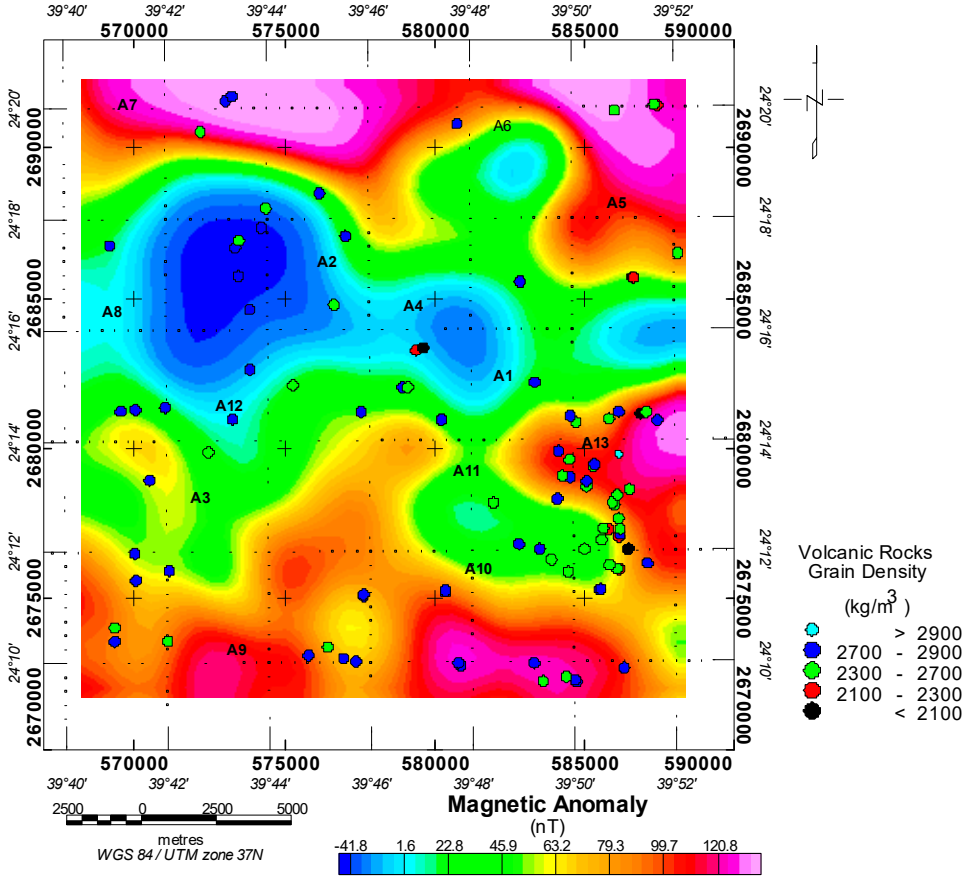

Figure 7. The magnetic anomaly map of the study region. A low magnetic susceptibility feature can be noticed within the central region of the study area. The location of the rock samples obtained for the density analysis [27] is plotted on the map.

2.2. Methodology

We obtained the profiles at prominent gravity anomaly locations across the study area to perform our initial 2D modeling with the Geosoft GMSYS™ software. The initial model, including the depth, shape, and density of the model layers, was comparatively obtained from the previously published density analysis of rock samples and models [27,28]. Hand-sized or larger samples of Harrat Rahat rocks (N = 527) were collected by geologists from the United States Geological Survey and were measured for their density and magnetic susceptibility [27]. The locations from which the rock samples were obtained are shown in Figure 7. Table 1 displays the profile parameters for the individual profiles.

2.3. Particle Swarm Optimization (PSO)

We adopted the PSO computation method, as proposed by Roy et al. [30]. The analysis of the gravity observations to invert basement topography is a nonlinear inverse problem [49]. Generally, the optimization techniques employed for any inversion include two basic types: (i) local optimization and (ii) global optimization. Proper initial and geologically reasonable model constraints are required for local optimization convergence to a global minimum, whereas global optimization is advantageous, since it can also provide uncertainty estimates [30]. The global optimization can be used to optimize the fault structure using the PSO of gravity data [47,68] to estimate the depth to the basement [30,39], to assess the model parameters using residual gravity anomalies [69], and to invert residual gravity anomalies above geological ensembles [70]. The attainment of the minimum of any objective function constitutes the ultimate goal for any optimization algorithm. The movement of each particle within the search space follows two methods:

exploration and exploitation. The search for a solution farther from the current solution within the search space defines the exploration, whereas, if the search area surrounds the present solution, towards improving it, this is termed exploitation. To achieve a faster convergence, a suitable balance between exploration and exploitation is obligatory for any optimization algorithm [30]. the PSO method was initially suggested after studying the behavioral pattern of birds and fish [71,72]. The conclusions determined were that every individual of the group or swarm benefits from the collective effort of the swarm, when the resource availability is random or unpredictable. The PSO was therefore adapted to solve the optimization of the continuous nonlinear functions by Kennedy and Eberhart [73]. In the present study, a Fourier domain depth profile representation and optimization with PSO for the depth varying density contrast, representative of most real geological scenarios, was utilized. The Fourier domain representation has been proven [30] to lessen the number of parameters for optimization and improve the computational time. The Fourier domain inversion is performed using the methods of Gao et al. [74], Chai and Hinze [75], and Cordell [76], and the inverse Fourier transform is employed for the depth profile estimation [30,77]. Detailed uncertainty appraisal analyses of the various synthetic models and real geological situations were conducted on this technique by Roy et al. [30], and the results were satisfactory. Therefore, we demonstrated an example application on a synthetic model, with and without noise, and thereafter proceeded to implement the technique on our gravity field data. Figure 8 summarizes the workflow followed for the successful implementation of the PSO in the present study.

Table 1. The profiles obtained across the anomaly body in the study area, with their corresponding azimuths.

Profile	Longitude (°)	Latitude (°)	Length (km)	Azimuth (°)
PP′	39.69 39.79	24.25 24.18	12.74	144.3
QQ′	39.71 39.85	24.28 24.20	16.89	145.6
RR′	39.74 39.87	24.30 24.22	16.35	145.8
SS′	39.76 39.86	24.33 24.27	13.52	150.4
TT′	39.83 39.85	24.32 24.16	16.37	83.1
UU′	39.77 39.82	24.33 24.16	18.13	43.5
VV′	39.69 39.87	24.25 24.25	18.53	0.1

A swarm describes a population of candidate solutions contained in the PSO. Each candidate solution is intended as a particle in the population and bears the parameter information of the model. Hence, the optimization problem has each particle as the candidate solution. Every potential solution to the optimization problem is hosted within the search space. Amid all the particles in the swarm, the best solution would be derived by the algorithm.

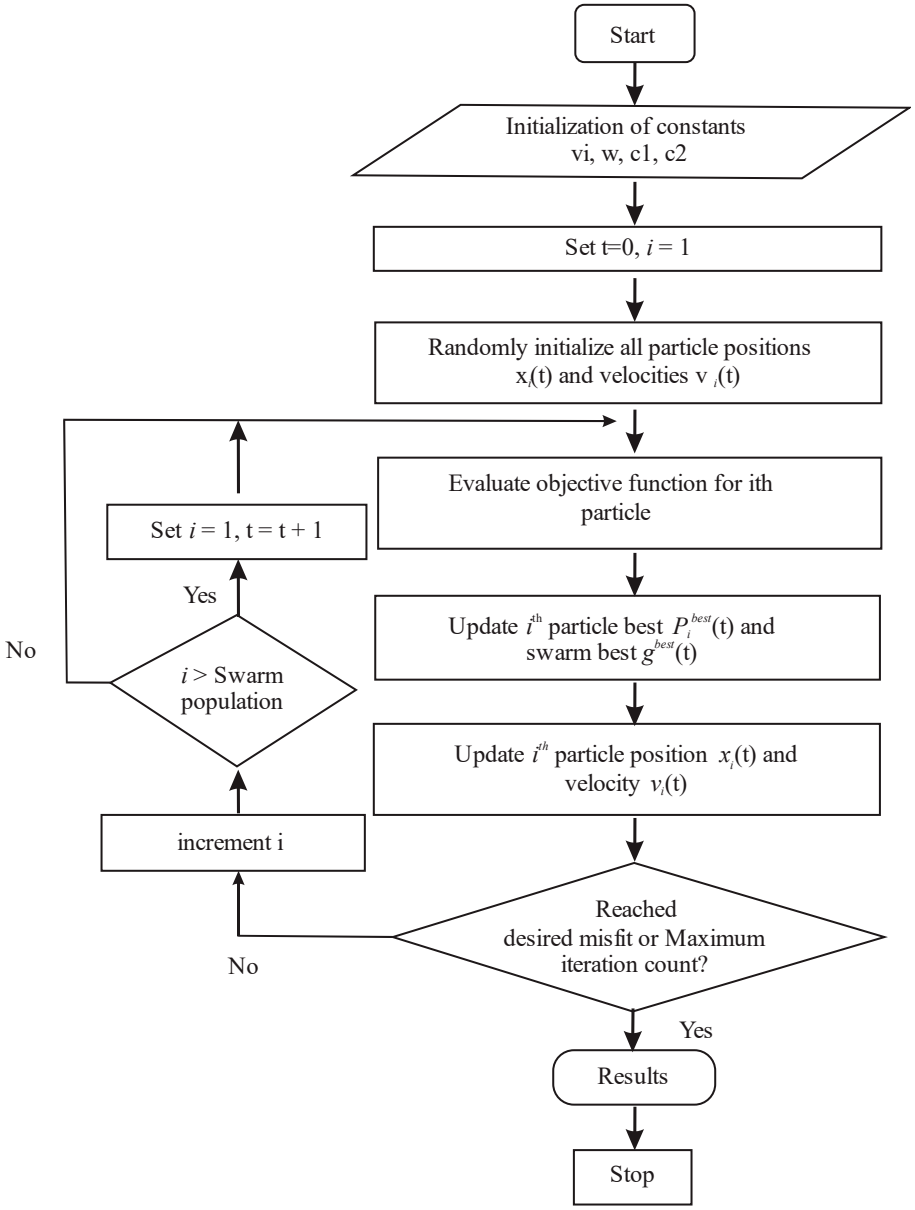

Figure 8. The flowchart for the PSO algorithm [30].

Consider an objective function $\boldsymbol{\Phi}\left(\vec{X}\right)$ having $\boldsymbol{D}$ parameters intended for optimization, with N particles dominating the search space; each particle is a set of $\boldsymbol{D}$ parameters evolving in time steps searching for an improved parameter set. $\vec{\boldsymbol{X}}_i(t)$ consisting of $\boldsymbol{D}$ parameters denotes the ith particle following the time step t, and can be represented as:

$$\vec{\boldsymbol{X}}_i(t) = \left[\vec{\boldsymbol{x}}_{1i}(t),\ \vec{\boldsymbol{x}}_{2i}(t),\ \vec{\boldsymbol{x}}_{3i}(t),\ \ldots,\ \vec{\boldsymbol{x}}_{Di}(t)\right], \text{where } i \in \{1,\ 2,\ 3,\ \ldots,\ N\} \tag{2}$$

From Figure 9, $\vec{\boldsymbol{X}}_i(t)$ denotes the ith particle position within the search space considering any discrete time step, with each having a velocity, $\vec{\boldsymbol{V}}_i(t)$.

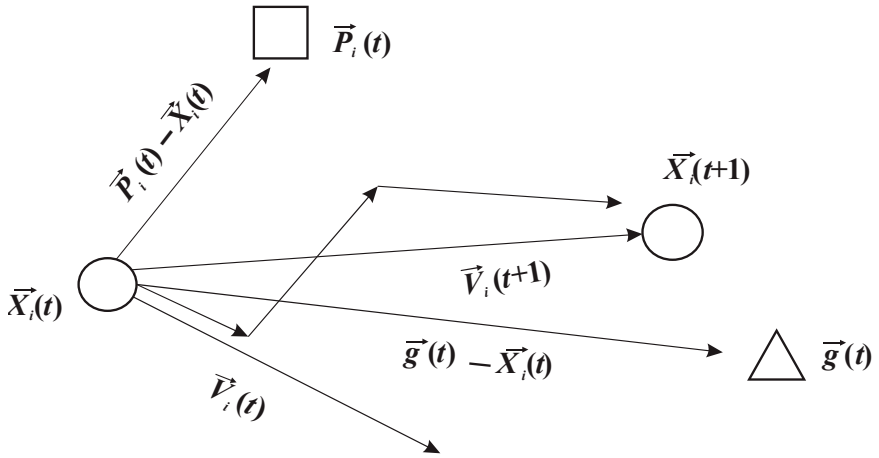

Figure 9. The vector representation of the position and velocity for the PSO. $\vec{P}_i(t)$ is the personal best of *i*th particle and $\vec{g}(t)$ is the global best of the entire swarm at the time step *t*. $\vec{X}_i(t)$ is the current position and $\vec{V}_i(t)$ is the current velocity of the *i*th particle at the time step *t*.

$\vec{X}(t)$ and $\vec{V}(t)$ possess similar dimensions; for each time step, the particle movement is represented by $\vec{V}(t)$. The particle best position ($\vec{P}_i^{best}$) is a point for a particular particle, for which the objective function is the minimum at every point of the discrete time step. The entire swarm also has a best position ($\vec{g}^{best}$). The velocity and position of each particle are updated after each time step and are mathematically represented as:

$$\vec{V}_i(t+1) = \omega\vec{V}_i(t) + c_1 r_1\left(\vec{P}_i^{best}(t) - \vec{X}_i(t)\right) + c_2 r_2\left(\vec{g}^{best}(t) - \vec{X}_i(t)\right) \quad (3)$$

$$\vec{X}_i(t+1) = \vec{X}_i(t) + \vec{V}_i(t+1) \quad (4)$$

Here, ω is the inertia weight, c_1 and c_2 are the acceleration coefficients, and r_1 and r_2 are the two random numbers in the range (0, 1). The term $c_1 r_1\left(\vec{P}_i^{best}(t) - \vec{X}_i(t)\right)$ is known as the cognitive component, $c_2 r_2\left(\vec{g}^{best}(t) - \vec{X}_i(t)\right)$ is known as the social component, and the inertia term is $\omega\vec{V}_i(t)$.($\vec{V}_i(t+1)$ is the new velocity vector and serves as obtaining the optimum parameter set of each particle by translating the position vector into a new location within the search space.

Here, ω, c_1, and c_2 are known as the control parameters for the PSO. The range for the inertia weight is chosen between 0.1 and 0.9, following the equations presented in the study of Roy et al. [30] and Perez and Behdinan [78]; the acceleration coefficients are $c_1 = 1.4$, $c_2 = 1.7$; the maximum number of iterations = 300; and the population size is 300. A further insight into the PSO procedures can be observed in the studies of Roy et al. [30], Nickabadi et al. [79], Xin et al. [80], Perez and Behdinan [78], and Malik et al. [81]. The objective function must be the minimum for the parameters in volvedin any optimization problem. For the present study, the error norm between the observed gravity data $g_z(x_i, z_i)$ and the gravity anomaly, due to the model, constitutes the objective function. Consider $\hat{O}$ as the operator for computing the gravity anomaly owed to any unrestricted depth profile $z(x_i)$, then the objective function is the following:

$$\Phi = \sum_{i=1}^{n} \left(g_z(x_i,\ z_i) - \hat{O}(z(x_i)) \right)^2$$
$$= \sum_{i=1}^{n} \left(g_z(x_i,\ z_i) - \hat{O} \left(a_0^z + \sum_{k=0}^{k<\frac{n}{2}} a_k^z cos\left(\frac{2\pi k x_i}{n\Delta x_i} \right) + b_k^z sin\left(\frac{2\pi k x_i}{n\Delta x_i} \right) \right) \right)^2 \quad (5)$$

where k and n are the optimization parameters corresponding to the number of Fourier harmonics and the number of observation points, respectively. The reconstruction of a depth, as well as the gravity profile from the Fourier domain, requires only a few dominating frequencies. Furthermore, a higher correlation exists between the power spectrum of the Fourier coefficients of a gravity anomaly and the corresponding depth profile for any vertically varying density distribution [30]. Therefore, the dominant frequencies that are used to describe the depth profile are the same as the dominant frequencies of the gravity anomaly.

2.4. The Euler Deconvolution of the Aeromagnetic Data

We evaluated the aeromagnetic anomaly data of the region and compared the results to the depths of the basement obtained from the gravity inversions. The magnetic potential field highlights the voluminous magnetic sources, such as those lying beneath a volcanic field, and therefore should be a reasonable proxy for the basement gravity variations [27]. The standard 3D Euler technique is founded on Euler's homogeneity equation—an equation relating a potential field, along with its gradient constituents to the source position, with a structural index, SI [82]. We took into account an exponential factor analogous to the ratio by which the potential field decreased with distance when a source with a given geometry was considered. For our computations, we adopted the standard 3D design of Euler's equation, as implemented by Geosoft Oasis Montaj software as:

$$x\frac{\partial T}{\partial x} + y\frac{\partial T}{\partial x} + z\frac{\partial T}{\partial x} + \eta T = x_o\frac{\partial T}{\partial x} + y_o\frac{\partial T}{\partial x} + z_o\frac{\partial T}{\partial x} + \eta b \quad (6)$$

where x, y and z represent the coordinates of a measuring point, x_o, y_o and z_o represent the coordinates of the source position, for which the total field is discerned at $x, y,$ and z; b represents a base level; η represents the structural index (SI); and T represents the total magnetic field. The source body type of interest determines the value of the SI [83]. As an example, Thompson [82], Reid et al. [84] and Abraham and Alile [85] proposed η = 0 for a contact, η = 1 (vertical dike or the edge of a sill), η = 2 (center of a horizontal or vertical cylinder), and η = 3 (center of a magnetic orb or dipole). Euler's equation for the magnetic data possesses a significant advantage because it is indifferent to the magnetic inclination, remanence, and declination, which constitute a constant in the anomaly function of any given model. For the present study, we selected an SI = 0 to achieve the identification of the possible contact depths and a window size of 0.5 km.

3. Results

Figure 10 displays the two-dimensional forward models with the observed and calculated gravity and magnetic responses. The error (misfit) of the models is also shown. The effects associated with the topography along the plane of the two-dimensional models were calculated and corrected for by GM-SYS during the modeling. GM-SYS is an extension of Geosoft Oasis Montaj (www.geosoft.com) and allows for the forward modeling of gravity and magnetic data in 2D or 2.75D [86,87]. The magnetic data was introduced in the modeling to provide additional constraints for the model depth results. The depth to the Proterozoic basement was adequately resolved from the gravity-magnetic modeling. Other varying sections of the basement were also identified and modeled with very minimal root-mean-square (RMS) errors.

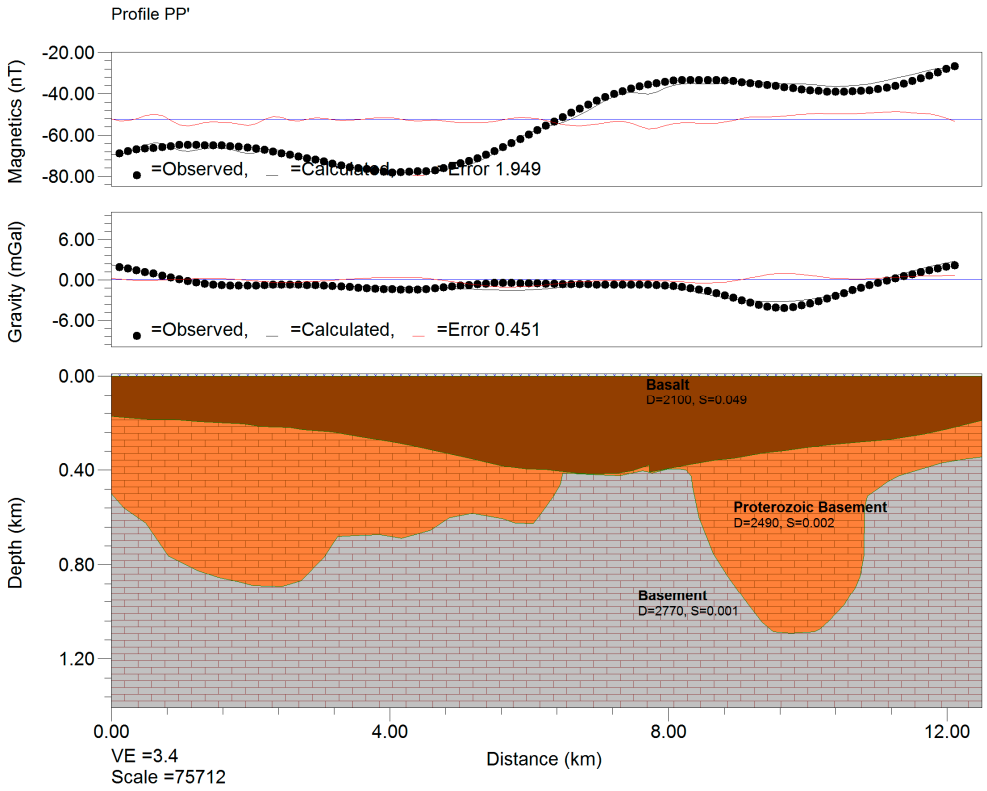

(**a**)

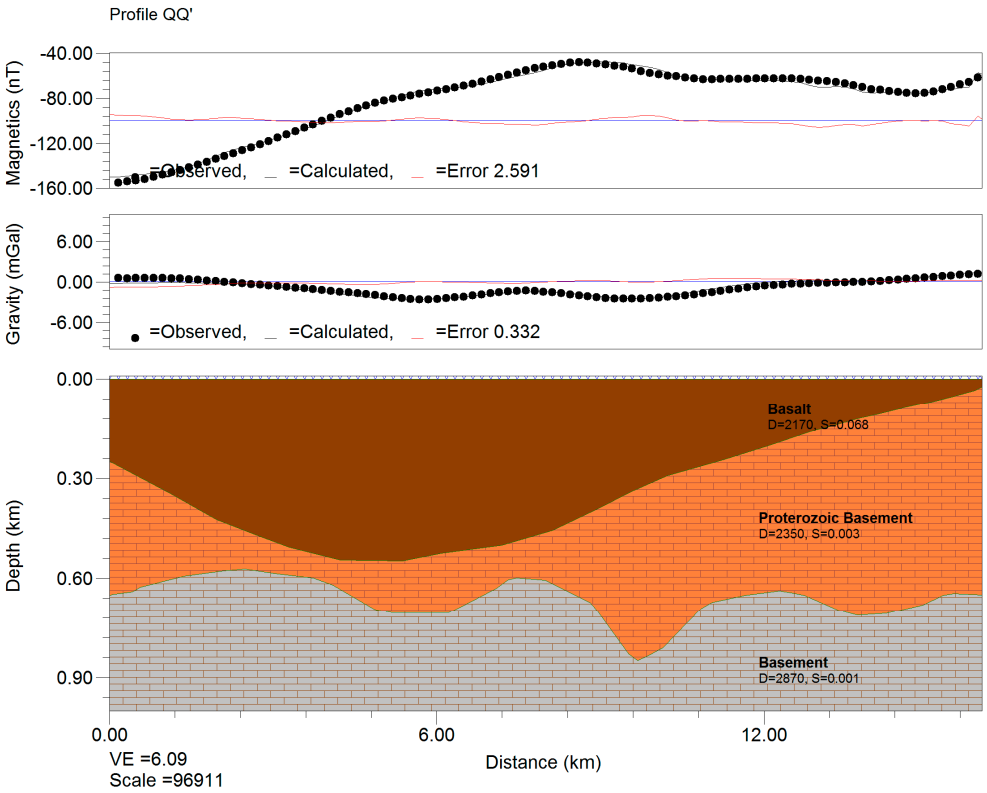

(**b**)

Figure 10. *Cont.*

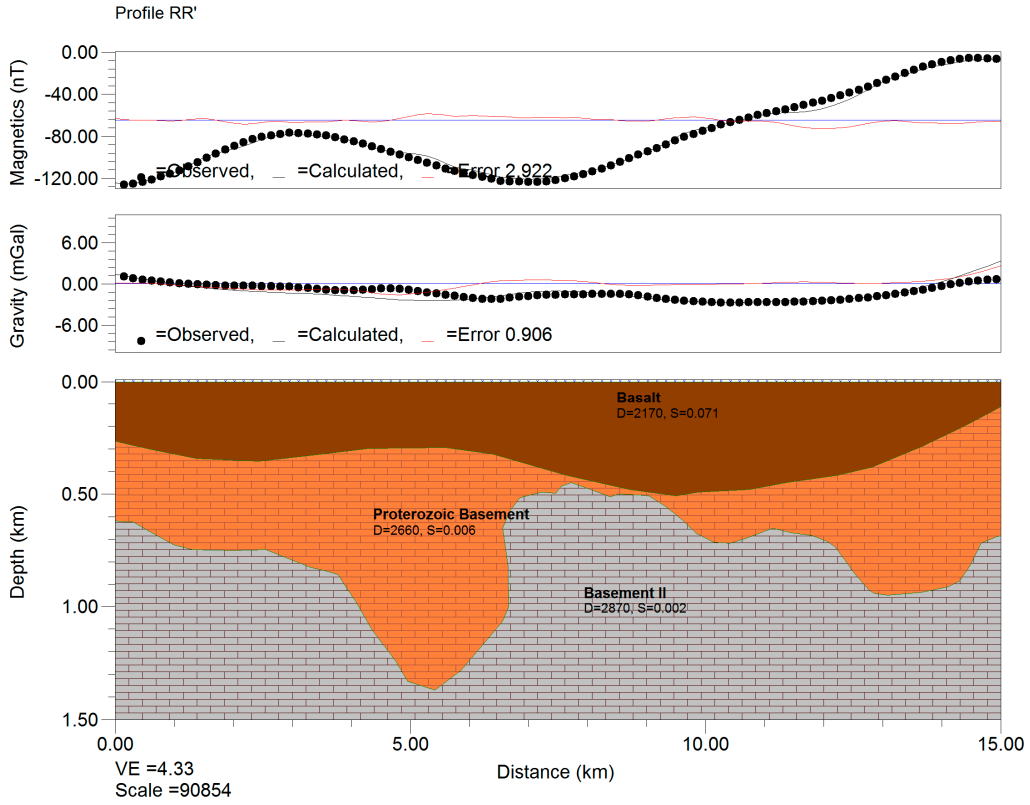

(**c**)

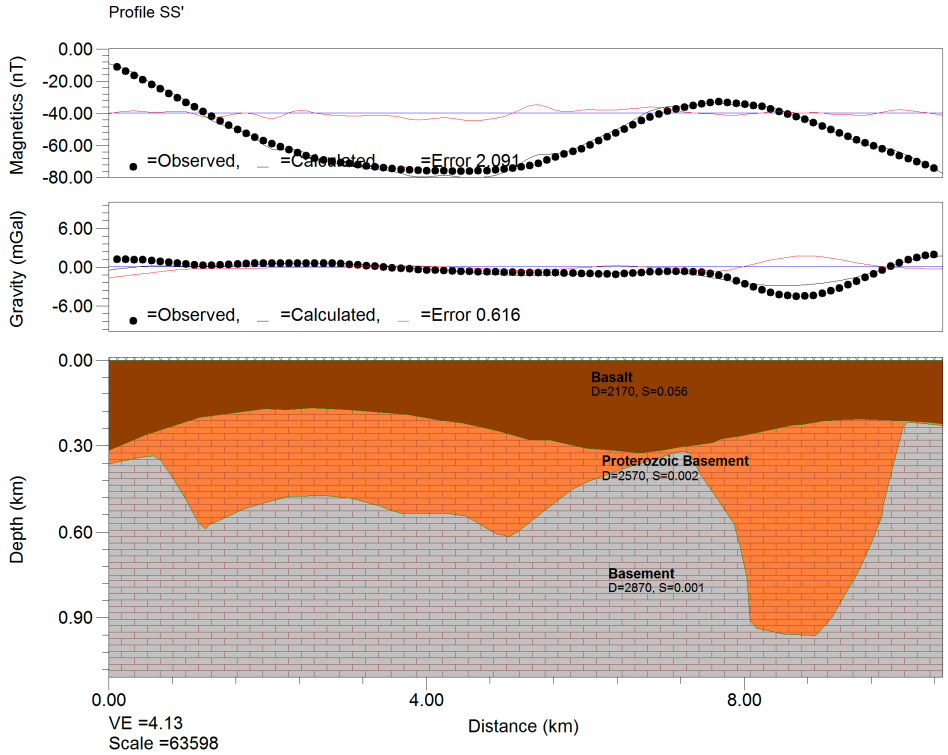

(**d**)

Figure 10. *Cont.*

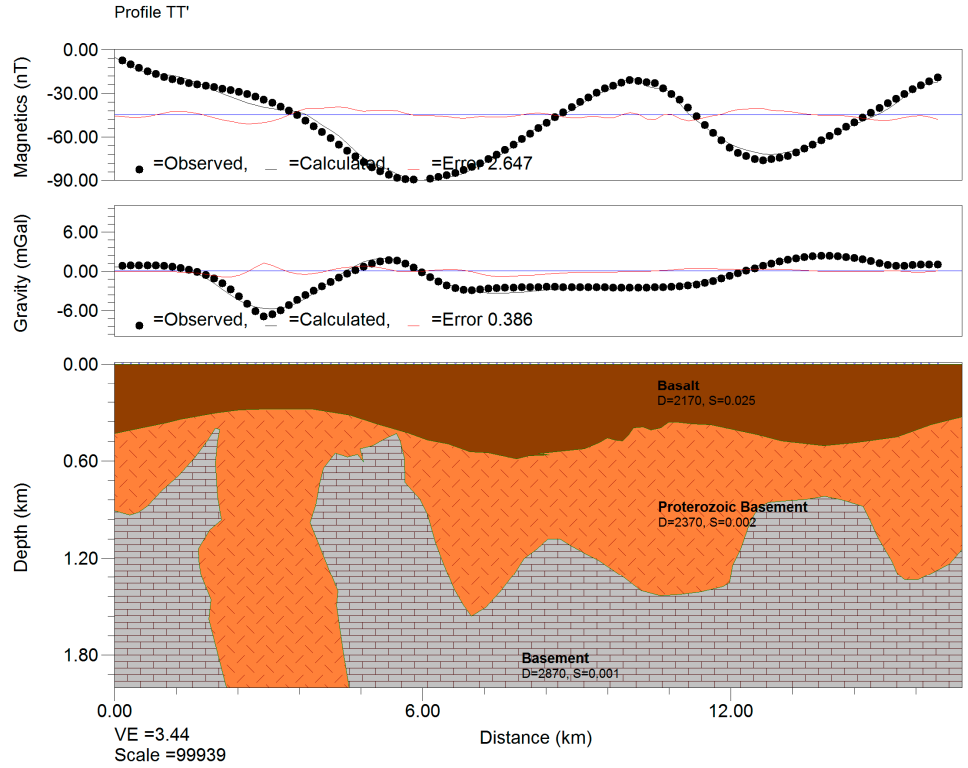

(**e**)

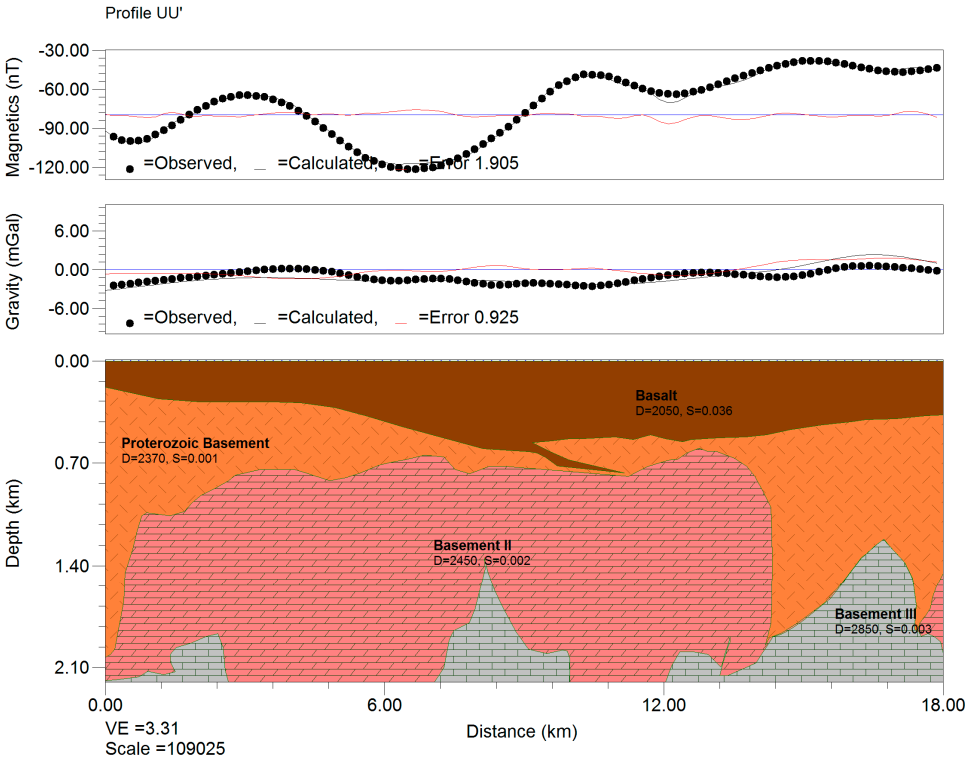

(**f**)

Figure 10. *Cont.*

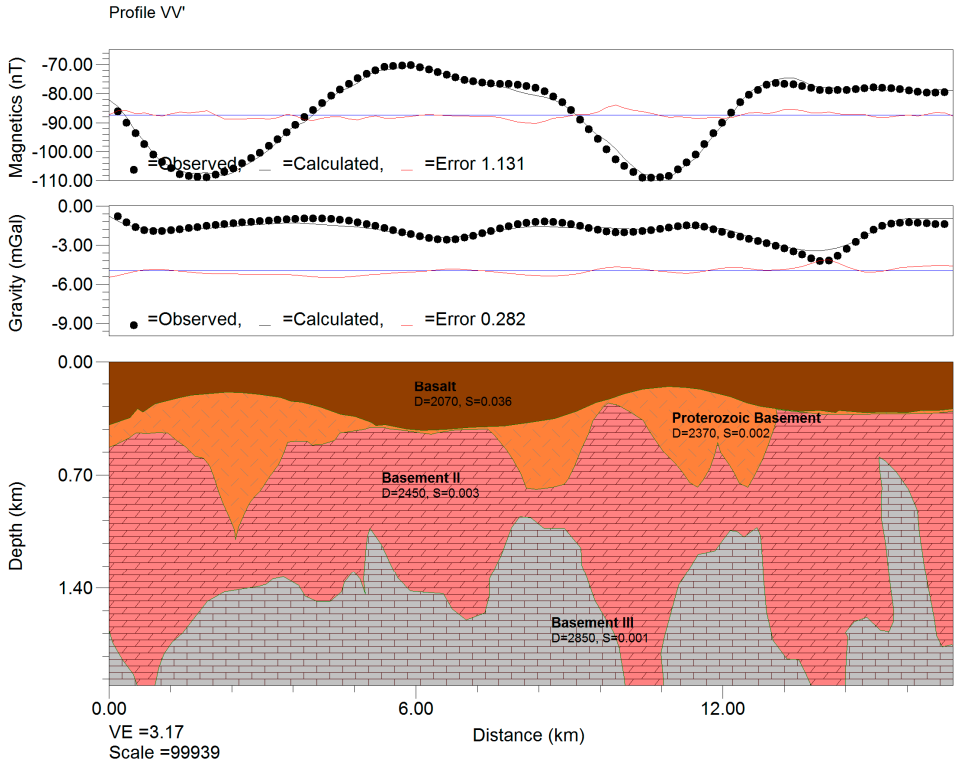

(**g**)

Figure 10. (**a**) A two-dimensional forward modeling result from the gravity and magnetic data obtained from Profile PP′.(**b**) A two-dimensional forward modeling result from the gravity and magnetic data obtained from Profile QQ′. (**c**) A two-dimensional forward modeling result from the gravity and magnetic data taken from Profile RR′. (**d**) A two-dimensional forward modeling result from the gravity and magnetic data taken from Profile SS′. (**e**) A two-dimensional forward modeling result from the gravity and magnetic data taken from Profile TT′. (**f**) A two-dimensional forward modeling result from the gravity and magnetic data taken from Profile UU′. (**g**) A two-dimensional forward modeling result from the gravity and magnetic data taken from Profile VV′.

The observational noise (which is always present in the data), noise introduced in gravity reduction for the complete Bouguer anomaly computation, and noise introduced in the regional trend suppression contribute to the inverse problem non-uniqueness and must always be taken into account in the results interpretation step [49]. The popular techniques used for the solution of this inverse problem are based on local optimization methods, either by the linearization of the problem and the use of linear algebra techniques (see [88], for example), or by the sequential application of the direct formulation (see [89], for example) [49]. The PSO algorithm, a global search method, exploits its excellent capabilities for the inverse problem uncertainty analysis to avoid the weak points of the local optimization methods, such as the dependence on the prior model, and the uncertainty analysis in nonlinear problems [49]. Roy et al. [30] tested the PSO formulation on various synthetic models of constant and varying density contrasts and obtained a good convergence in both cases. By using a depth varying density contrast ($-300--385$ kg/m^3), we showed a synthetic model (Figure 11a) for the depth profile of a sedimentary basin, together with its matching gravity anomaly. Figure 11b shows the model results with added Gaussian noise.

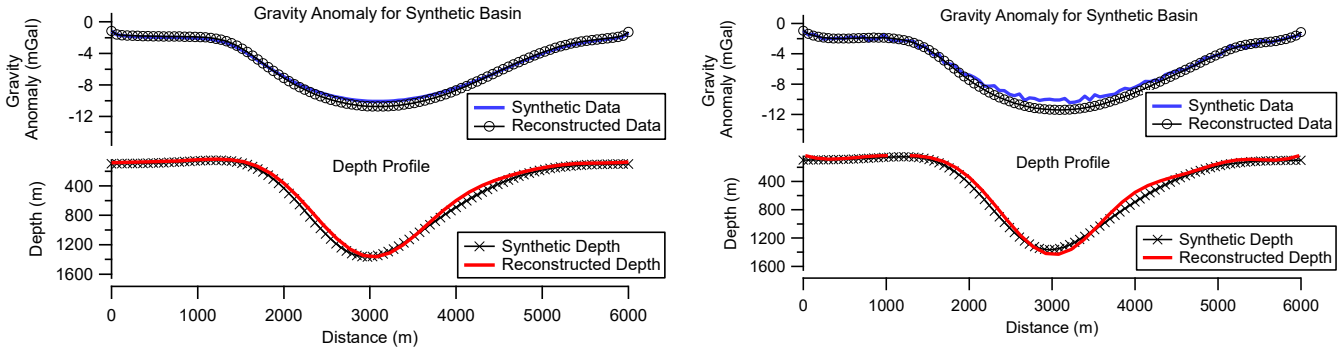

Figure 11. (**a**) Synthetic gravity anomaly model plots showing the reconstructed data and corresponding depths from the PSO computations. (**a**) A model plot without added noise, and (**b**) the model results with added Gaussian noise. The density contrast was varied between -300 and -385 kg/m^3.

Figure 12 displays the results from the subsequent PSO computations on the gravity data from profiles (7), obtained across the region of investigation. Seven profiles were drawn across the notable anomalies in the study area.

Table 2 presents the number of parameters of the Fourier coefficients for each of the selected depth profiles. The root-mean-square error (RMSE) values of the computed gravity anomalies are also displayed.

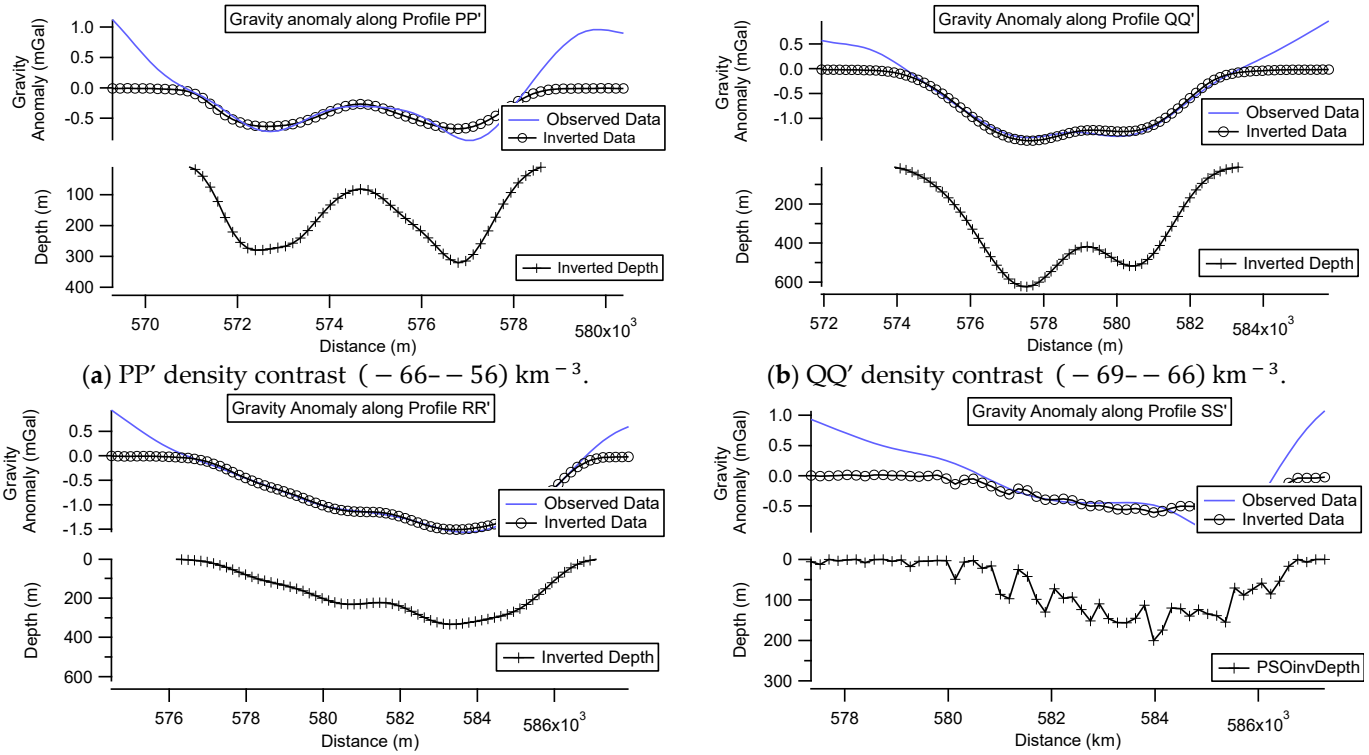

Figure 12. *Cont.*

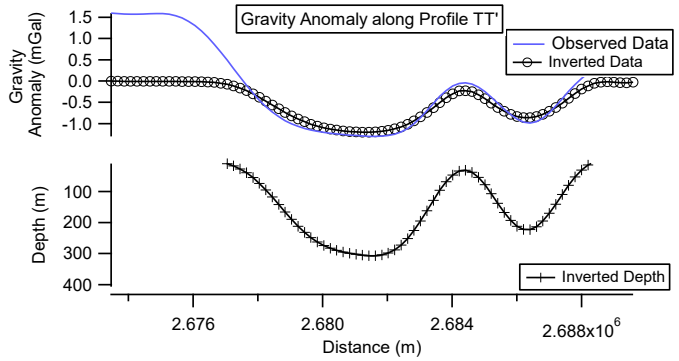

(**e**) TT′ density contrast (−110–−90) km^{-3}.

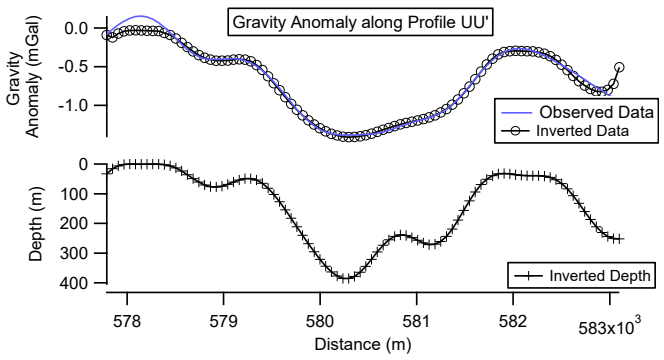

(**f**) UU′ density contrast (−130–−105) km^{-3}.

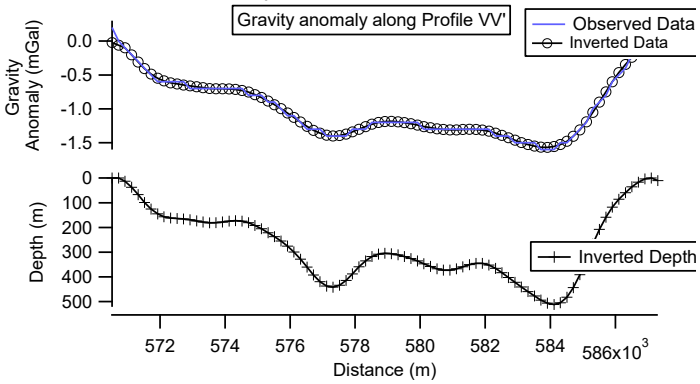

(**g**) VV′ density contrast (−95–−75) km^{-3}.

Figure 12. The observed gravity anomalies from the profiles obtained across the study area. The solid blue line presents the observed gravity field along the profiles, the line-through-circles symbol represents the inverted gravity field, and the line-through-crosses symbol in the lower panel represents the inverted depths realized from the PSO computations. The density contrast ranges between −130 and −60 kg/m^3. The inverted gravity data and depth results were obtained using PSO computations along Profiles PP′ (**a**), QQ′ (**b**), RR′ (**c**), SS′ (**d**), TT′ (**e**), UU′ (**f**), and VV′ (**g**).

Table 2. The predicted top basement geometry parameters with the depth range and mean depth results. The RMSE in the gravity inversion is also represented for the individual profile computations.

Profile	No. of Parameters	RMS Error in Gravity Anomaly (mGal)	Depth Range (m)	Mean Depth (m)
PP′	19	0.215391	320.59	121.29
QQ′	12	0.130457	624.29	224.18
RR′	12	0.098459	333.75	146.26
SS′	99	0.212882	200.54	65.04
TT′	11	0.241633	306.96	115.14
UU′	14	0.046893	385.77	142.69
VV′	18	0.033018	511.41	269.83

A final comparison of the depths to basement obtained using the PSO method and GM modeling procedure is presented on the contour plots in Figure 13.

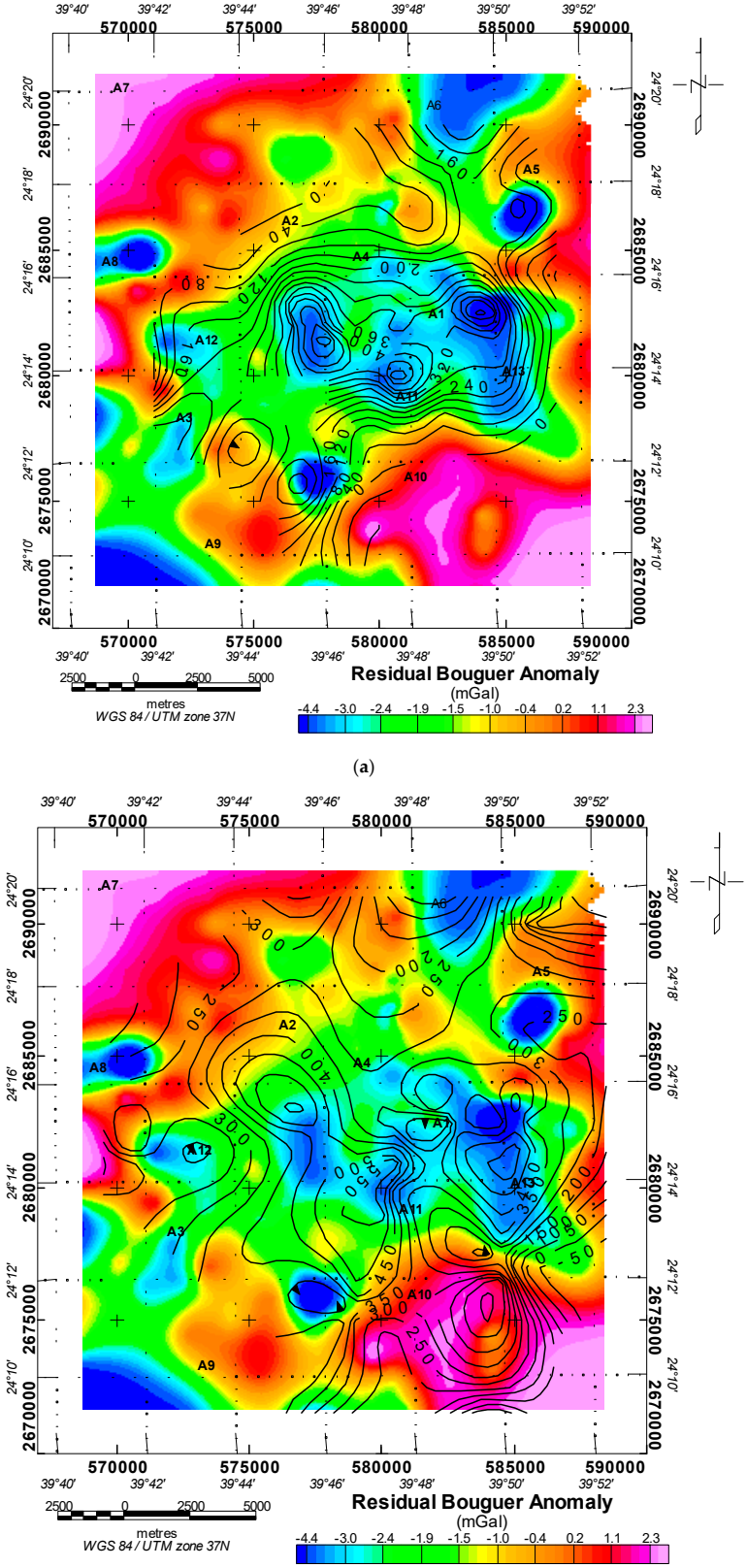

(**a**)

(**b**)

Figure 13. (**a**) The contour plot of the depths (m) to basement realized from the PSO computations superimposed on the residual gravity anomaly map of the region. (**b**) The contour plot of the depths (m) to basement realized from the GM modeling computations superimposed on the residual gravity anomaly map of the region.

Figure 14 shows the results of the Euler deconvolution depth computations performed to compare the depth results realized from the PSO computations.

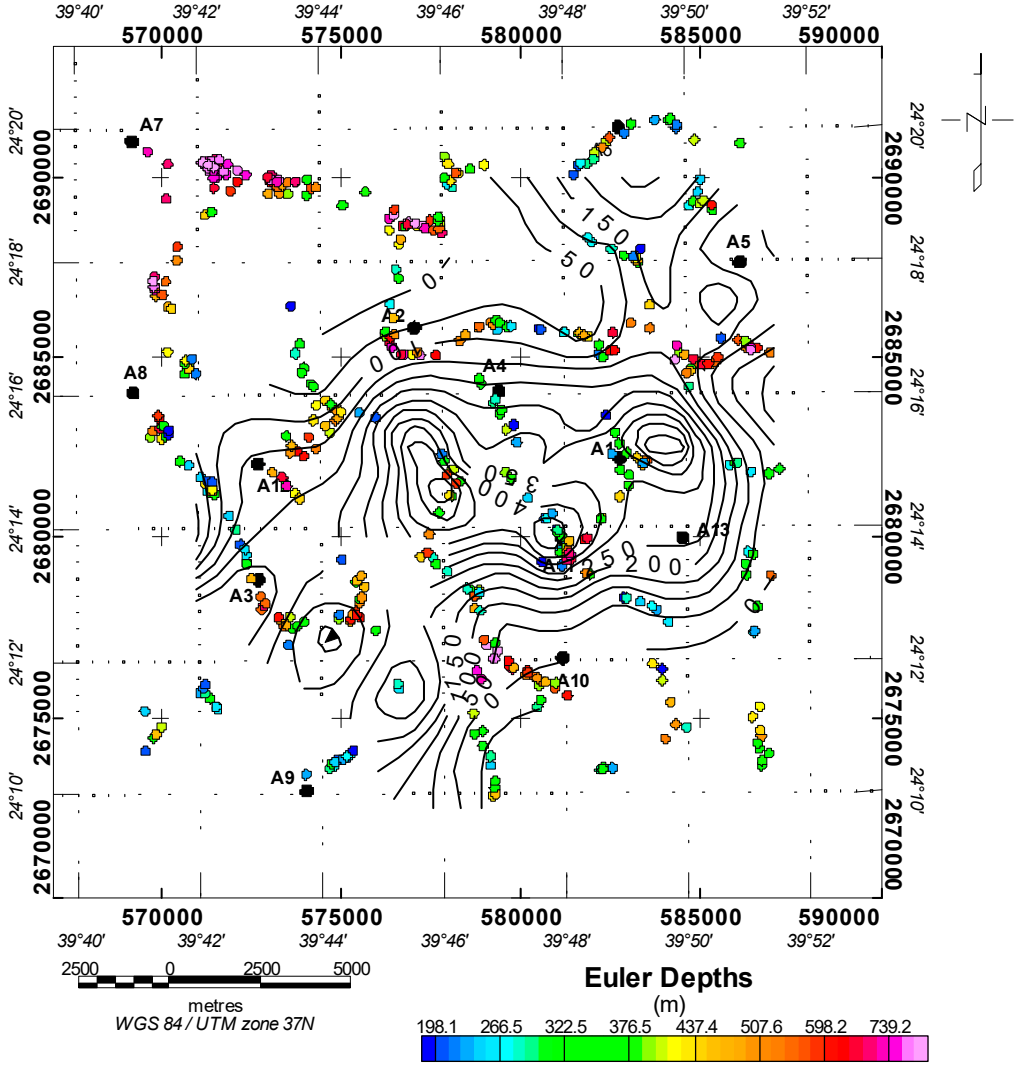

Figure 14. A comparison of the basement depth (m) estimates between the Euler deconvolution and PSO-derived depths. The Euler depths range between 135–695 m within the anomalous region of the study area.

The depths derived from the three-dimensional Euler deconvolution of the aeromagnetic anomalies were obtained solely from processing the aeromagnetic data for the contact sources and their magnetic trends, and bears its unique properties and effects, different from the two-dimensional GM- and PSO-derived depths. Nevertheless, we made a very rough comparison of the depths derived from the three methods (Euler, GMSYS, and PSO). The contact source depths from the Euler deconvolution were gridded to extract the rough estimates of the point depths. The depths that were extracted from the three methods along the established profiles were plotted for statistical evaluations (Figure 15). The determined depth ranges of the three methods were at a confidence level of 95%. The average depths from the graphical representation were also determined and extracted for the map contouring (Figure 16).

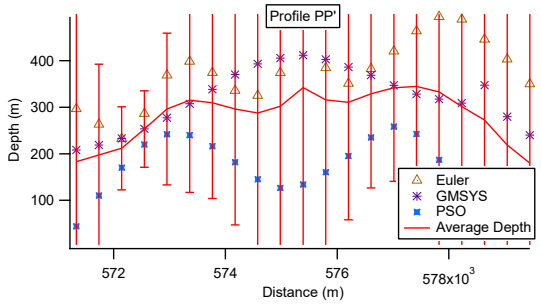

(**a**)

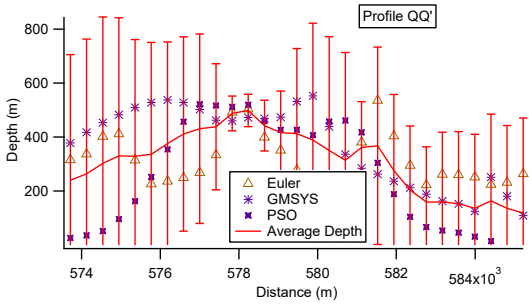

(**b**)

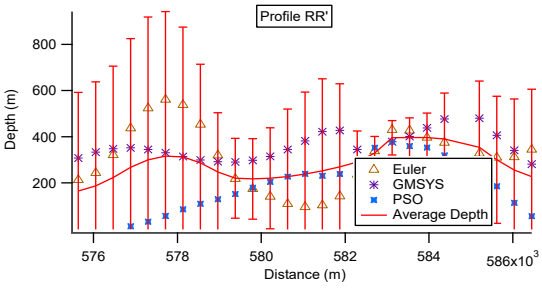

(**c**)

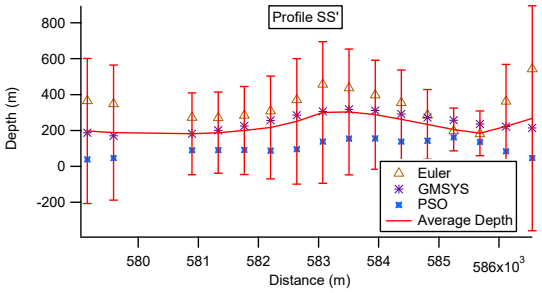

(**d**)

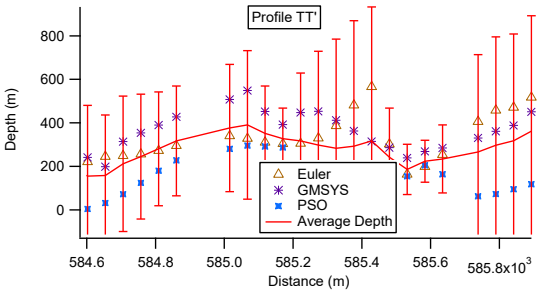

(**e**)

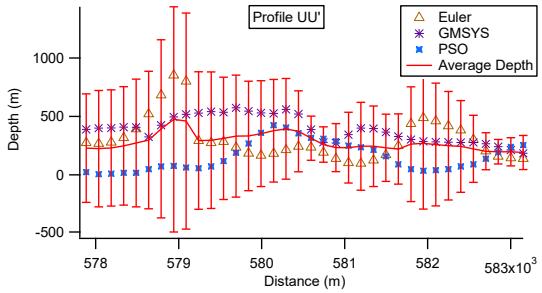

(**f**)

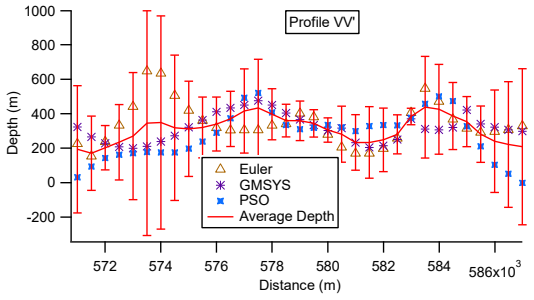

(**g**)

Figure 15. The graphical plot for the comparison of the depths from the three methods (Euler, GMSYS, and PSO). (**a**) Graphical depth plots for Profile PP′. (**b**) Graphical depth plots for Profile QQ′. (**c**) Graphical depth plots for Profile RR′. (**d**) Graphical depth plots for Profile SS′. (**e**) Graphical depth plots for Profile TT′. (**f**) Graphical depth plots for Profile UU′. (**g**) Graphical depth plots for Profile VV′.

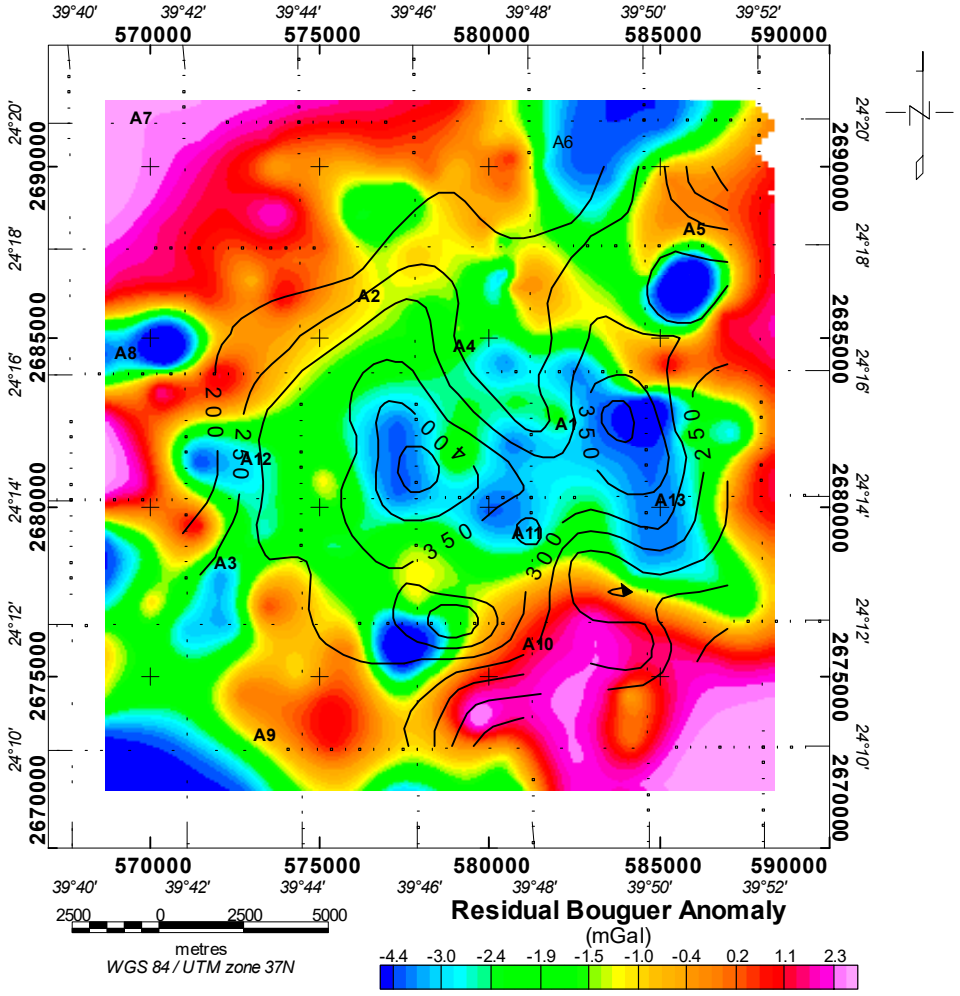

Figure 16. The contour plot of the average depths derived from the three methods. The compared averages range from 110–506 m, with deeper depths obtained at the central region of the study area.

4. Discussion

The residual gravity anomalies superimposed on the geology map (Figure 6) of the study area trace the sources of the gravity lows as being located mostly below the olivine basalt with a minor quantity of hawaitte and mugearite rocks. Residual gravity lows (<−3.0 mGal) are significant in the central (A4) and eastern regions (A13) of the study area, and can indicate a significant low-density structure within the subsurface in the basement. The observations [27] suggested that gravity lows within the region were also caused by sources beneath the volcanic field. To examine and confirm the presence of an anomalous body within the study area, we analyzed the aeromagnetic data of the study area (Figure 7). Low magnetic anomalies can be noticed in the central region of the map, which, in comparison to the gravity anomaly map (Figure 5), confirms the existence of an anomalous body within the subsurface at the study area. Low magnetic anomalies (<22 nT) are noticeable around the A1–A4 regions and extend (in like manner as the gravity lows) east-western at the central region, confirming the existence of an anomalous magnetization body in the region. In general terms, this anomalous body could hint at a structural unit with a geothermal energy potential in the area. A significant self-sealing exists at the top of the geothermal reservoir in Harrat Rahat, resulting in the lack of hydrothermal manifestations in the region [20]. The location and orientation of this anomalous body informed our choice of profile samplings (Figure 5).

Figure 10 shows the modeling results from a combination of gravity and magnetic data. The depth analysis results shown in Figure 10a imply a thick depositional layer (with

a depth reaching 350 m) at the center of Profile PP′, which decreases away from the center. The basin-shaped formation of the deposited basalt unit provides hints of the general shape of the subsurface and basement topography along with Profile PP′. A variation of the subsurface density structures could also be noticed in the model, having explicit density and magnetic properties. We believe that the existence of these subsurface intrusions within the Proterozoic basement is significant towards viable geothermal energy potentials at depths within the basin, especially in the deeper regions of the basin. A continuation of a basin-like structure of basaltic flows is also noticed in the model along Profile QQ′, with a maximum depth to the Proterozoic basement reaching 570 m (Figure 10b). The basin-like structure may indicate the existence of a geothermal reservoir in the area. Further examination also shows the Proterozoic basement topography decreasing in depths away from the profile center and pinches out at Q′ (which is located within the region with high gravity anomalies (Figure 7)), similar to Profile RR′ that shows model depths of ~500 m (Figure 10c) at the location with low residual gravity anomalies. Here, our modeling results suggest the presence of intrusions within the Proterozoic basement. The proximity of the intrusions to the base of the basaltic deposition could be responsible for the low magnetic anomalies, whereas the gravity lows could indicate the presence of a less dense subsurface reservoir within the region. These are good indicators of favorable geothermal energy prospects at the location. Previously, Pellaton [90] reported a sub-volcanic basement depth of ~500 m obtained from a geophysical analysis in the HRVF region.

Profile SS′ (Figure 10d) appears to be located on the boundary of the isolated anomalous structure within the study area. The top basement depth or thickness of the basaltic flow range is 100–300 m. These shallow depths correspond to the area with higher gravity anomaly values. We suspect this region to provide some sort of barrier to the basaltic flow being investigated in this study for its high geothermal potentials. Profile TT′ (Figure 10e) also confirms the results obtained, along with the parts of Profile SS′. The depths to the basement range between 200–570 m, as the profile intersects the major gravity lows within the identified singular body. A greater thickness of basaltic lava flows and the modeled intrusions within the subsurface at this location may indicate a high geothermal potential of this region. The lava succession of Harrat Rahat sits above an irregular surface on the Proterozoic basement, where aeromagnetic and gravity data indicate that it varies in thickness from 100 m near the margins of the Harrat to as deep as 300 to 500 m at the center [1]. Profile UU′ (Figure 10f) was obtained across the central region of the anomalous body under consideration. Depth-to-basement estimates show significant intrusions within the Proterozoic basement of variable density and magnetization. The density variations within the Proterozoic basement are possibly due to crustal modification by volcanic processes. For example, intrusions or partial melts can be possible sources of the gravity lows in the HRVF region [24,27]. Dike swarms intrude all of the Proterozoic units and are most prevalent west of Harrat Rahat [27,90,91]. The depth to the basement follows previous depths obtained along other profiles crossing the same location in this study. The larger depths to the basement reach 680 m and a significant isolated subsurface structure is suspected within the basement, which could be responsible for both lower gravity and magnetic anomalies in the area. We propose this region along Profile UU′ for further geothermal prospecting, as the location may possess significant prospects for geothermal energy exploration. Our proposal is corroborated by the depth results obtained from the modeling results of Profile VV′, with a very similar depth to the basement outcomes.

The model results from the synthetic gravity analysis (Figure 11) demonstrate the viability of the PSO technique to recover the true depths of the model, even with the introduction of noise (Figure 11b). Therefore, we applied the PSO technique to our profile data in the study area. The modeled basement geometry for Figure 12a–g matched the observed gravity residual Bouguer anomaly data, following the observed gravity anomaly data with the root-mean-square (RMS) error of 0.03–0.20 mGals (Table 2). The depths to the basement obtained using the PSO technique along these profiles ranged between 10–624 m and were found to be concurrent with the depths to the Proterozoic basement

realized from the GM modeling. The largest depth range agrees, to some extent, with the 500–600 m depths realized by Langenheim et al. [27] and differs significantly from the 1000–2000 m depth estimates determined by Aboud et al. [28] (from the Euler deconvolution of aeromagnetic data).The gravity inversion using the PSO method along Profiles UU′ and VV′ running across the major gravity lows within the central region indicates similar values of depth to the basement, with the data misfit of 0.03 mGals. Our gravity inversion result shows greater depths reaching 624 m, corresponding to the regions with very low residual gravity anomalies. This can be significant for further geothermal investigations as this could represent a region where the metamorphosed rock unit may be related to hydrothermal alteration. Roobol et al. [15] identified a 3.2 km long line of weak fumaroles adjacent to the 1256 A.D. historic lava flow with associated seismic activity from 1986 to 1988, and also reported that several individual water wells in the region had anomalously high temperatures of up to 53 °C, consistent with geothermal processes.

A further comparison is made from the contour plots of the depths to basement obtained using the GMSYS and PSO gravity inversion methods (Figure 13). The modeled basement is represented as contour lines on the residual Bouguer gravity anomaly maps. The regions of the study area with deeper depths (>500 m) agree with each other as well as the regions with shallow depths. Slightly greater depths were observed with the GMSYS models, when compared to the depths realized from the PSO computations; nevertheless, both methods adequately agreed on the locations with deeper depths, at the central and east-western regions of the study area. Greater depths to the basement (slightly > 600 m) (Figure 13) are located at longitude 39.77° E and latitude 24.25° N. We noticed a depth trend (EW) in the central region of the study area, with a depth to the basement ranging from 150–620 m and located between the longitudes of 39.74–39.85° E and latitudes of 24.22–24.27° N. We propose this region for further geothermal exploration, as it should deliver higher prospects for geothermal energy exploitation.

Comparable depth information was also realized from the three-dimensional Euler deconvolution depth estimates and the PSO depths (Figure 14). The depths to basement from the Euler deconvolution ranged between 50–810 m generally, and between 135–695 km at the region with an anomalous density contrast. Good clustering of the Euler depths follows various trends (NS, NW–SE, and EW) and could hint at the possible existence of subsurface contact sources (faults/fractures) at depths, trending with these directions. At the northern regions of the study area (around A1 − A4 − A5), clustered Euler solutions could be observed(NE_SW and EW) defining the boundaries of the anomalous subsurface density structure concurrently with the PSO depths. This can also observed at A3 and A10 regions. The locations with deeper Euler depths (for example, southwards at A10) between 437 and 598 m, agree with the PSO depths (~500 m) at the location. Similar deductions are also noticed at the central or southeastern regions of the study area, with depths varying between 300 and 600 m. Shallow depths (50–280 m) are noticeable in the northern and northwestern regions from the PSO depths, however Euler depths estimated for contact sources at these locations are slightly higher (ranging 250–300 m). Deeper depths to the basement realized from these computations are supportive of a geothermal system within the HRVF, and their variously identified and mapped regions are recommended for further geothermal investigations.

Depths obtained from the three-dimensional Euler deconvolution were derived solely from the processing of aeromagnetic data, and a combination of gravity and aeromagnetic data was used in the GMSYS forward modeling. The depths from the PSO inversion of the gravity data for the known density distributions were achieved from an automated parameter selection criterion. These depths are bound to appreciably vary from each other. Nevertheless, the depth range of these three methods indicates a common depth range in the study area, although with some notable individual variations. An average depth estimation of the three methods, evaluated at a confidence interval of 95%, was made for comparison. A graphical representation of the depths derived from the three methods (Euler, GMSYS, and PSO) is shown in Figure 15. A deviation of some Euler

depth estimates from the PSO depths at some locations is expected, given the different datasets used, and the excessive interpolation effected in the gridding of the Euler depths. This was particularly noticeable for the profiles obtained at the hypothesized boundary of the anomalous density structure (Figure 15a,c). We suspect that the structural index (SI = 0) utilized for the Euler depth estimates, which investigates the source contacts, could have identified the possible contact sources to include faults or fracture structures with corresponding depth information. While we used the depth information from the Euler deconvolution for comparison purposes, we were also cautious of its applicability and coverage, along with the various profiles. This was because of the wider solution gaps resulting from the Euler deconvolution depths solution plot (Figure 14). All methods agreed on a depth range between 0 and 800 m at the study area; Figure 16 presents a contour plot of the average depth from the three methods, notwithstanding the peculiarity and variability of the methods. All methods agreed on the locations with deeper basement depths within the study area, and provided educated depth-to-basement estimates at the study area.

5. Conclusions

Our assessment of the geothermal energy prospects at the northern part of the HRVF has shown viable prospects for further exploration of geothermal energy. The model results suggest the presence of intrusions within the Proterozoic basement, and the close proximity of the intrusions to the base of the basaltic deposition may be accountable for the low magnetic anomalies in the region. The gravity lows could indicate the presence of a less dense subsurface reservoir within the region. These are acceptable pointers to a favorable location with viable geothermal energy prospects. The three-dimensional Euler deconvolution processing for contact sources shows possible subsurface fault structures trending in the NE–SW, EW, NW–SE, and N–S directions, with corresponding depths reaching 695 m in the central region of the study area. The estimated depths to the basement using the gravity inversion method based on the PSO technique provided depth-to-basement estimates of on average of ~620 m within a low gravity anomalous subsurface structure in the study area. The thickness of the basaltic lava flows and the modeled intrusions within the subsurface at this location may indicate the high geothermal potential of this region. The depths derived from the two-dimensional gravity inversion using the PSO method are comparable with the estimated depths obtained using two-dimensional forward modeling and the three-dimensional Euler deconvolution of aeromagnetic data. A comparison of the three methods adopted for our evaluations confirmed that the region with a deeper PSO resolved the depths to the basement. The results indicate more accurate locations for future geothermal energy exploration within the HRVF.

Author Contributions: Conceptualization, F.A., E.M.A. and E.A.; methodology, E.M.A., E.A. and M.R.; software, F.A. and E.M.A.; validation, F.A., E.M.A. and E.A.; formal analysis, E.M.A. and E.A.; investigation, E.M.A., E.A. and M.R.; resources, F.A., E.M.A., E.A. and M.R.; data curation, F.A., E.M.A. and E.A.; writing—original draft preparation, E.M.A. and E.A.; writing—review and editing, F.A., E.M.A., E.A. and M.R.; visualization, E.M.A.; supervision, F.A. and E.A.; project administration, F.A.; funding acquisition, F.A. and E.A. All authors have read and agreed to the published version of the manuscript.

Funding: This research work was funded by the Institutional Fund Projects under grant no IFPNC-001-145-2020. Therefore, the authors gratefully acknowledge the technical and financial support from the Ministry of Education and King Abdulaziz University, Jeddah, Saudi Arabia.

Institutional Review Board Statement: Not applicable.

Informed Consent Statement: Not applicable.

Data Availability Statement: The data presented in this study are available on request from the corresponding author. The data are not publicly available due to privacy restrictions.

Acknowledgments: The Geohazard Research Center of King Abdulaziz University (KAU), Jeddah, is acknowledged for their support throughout the course of this study. Our gratitude also goes to the anonymous reviewers and editors for their useful comments, which enhanced our manuscript.

Conflicts of Interest: The authors declare no conflict of interest.

References

1. Al-Amri, A.M.; Mellors, R.; Harris, D.; El-Sayed, K.A. *Geothermal and Volcanic Evaluation of Harrat Rahat, Northwestern Arabian Peninsula*; Profect No.: 11-SPA 2208-02; National Plan for Science, Tech. & Innovation; King Saud University: Riyadh, Saudi Arabia, 2016.
2. Al-Shijbi, Y.; El-Hussain, I.; Deif, A.; Al-Kalbani, A.; Mohamed, A.M.E. Probabilistic Seismic Hazard Assessment for the Arabian Peninsula. *Pure Appl. Geophys.* **2019**, *176*, 1503–1530. [CrossRef]
3. Zahran, H.M.; Sokolov, V.; Roobol, M.J.; Stewart, I.C.F.; Youssef, S.; Elhadidy, M. On the development of a seismic source zonation model for seismic hazard assessment in western Saudi Arabia. *J. Seism.* **2016**, *20*, 747–769. [CrossRef]
4. Wilson, J.W.P.; Roberts, G.G.; Hoggard, M.J.; White, N.J. Cenozoic epeirogeny of the Arabian Peninsula from drainage modeling. *Geochem. Geophys. Geosystems* **2014**, *15*, 3723–3761. [CrossRef]
5. Niazi, M. Crustal Thickness in the Central Saudi Arabian Peninsula. *Geophys. J. Int.* **1968**, *15*, 545–547. [CrossRef]
6. El-Hussain, I.; Al-Shijbi, Y.; Deif, A.; Mohamed, A.M.E.; Ezzelarab, M. Developing a seismic source model for the Arabian Plate. *Arab. J. Geosci.* **2018**, *11*, 435. [CrossRef]
7. Deif, A.; Al-Shijbi, Y.; El-Hussain, I.; Ezzelarab, M.; Mohamed, A.M. Compiling an earthquake catalogue for the Arabian Plate, Western Asia. *J. Southeast Asian Earth Sci.* **2017**, *147*, 345–357. [CrossRef]
8. Stern, R.J.; Johnson, P. Continental lithosphere of the Arabian Plate: A geologic, petrologic, and geophysical synthesis. *Earth-Sci. Rev.* **2010**, *101*, 29–67. [CrossRef]
9. ArRajehi, A.; McClusky, S.; Reilinger, R.; Daoud, M.; Alchalbi, A.; Ergintav, S.; Gomez, F.; Sholan, J.; Bou-Rabee, F.; Ogubazghi, G.; et al. Geodetic constraints on present-day motion of the Arabian Plate: Implications for Red Sea and Gulf of Aden rifting. *Tectonics* **2010**, *29*, TC3011. [CrossRef]
10. Berthier, F.; Demange, J.; Iundt, F.; Verzier, P. *Geothermal Resources of the Kingdom of Saudi Arabia*; Saudi Arabian Deputy Ministry for Mineral Resources Open-File Report BRGM-OF-01-24; Ministry of Petroleum and Mineral Resources: Jiddah, Saudi Arabia, 1981; p. 116.
11. Rehman, S.; Shash, A. Geothermal Resources of Saudi Arabia—Country Update Report. In Proceedings of the World Geothermal Congress 2005, Antalya, Turkey, 24–29 April 2005.
12. Rehman, S. Saudi Arabian Geothermal Energy Resources—An Update. In Proceedings of the World Geothermal Congress 2010, Bali, Indonesia, 25–29 April 2010.
13. Demirbas, A.; Alidrisi, H.; Ahmad, W.; Sheikh, M.H. Potential of geothermal energy in the Kingdom of Saudi Arabia. *Energy Sources Part A Recover. Util. Environ. Eff.* **2016**, *38*, 2238–2243. [CrossRef]
14. Al-Dayel, M. Geothermal resources in Saudi Arabia. *Geothermics* **1988**, *17*, 465–476. [CrossRef]
15. Roobol, M.J.; Bankher, K.; Bamufleh, S. *Geothermal Anomalies along the MMN Volcanic Line Including the Cities of Al Madinah Al Munnawwarah and Makkah Al Mukkarramah*; Saudi Geological Survey: Jeddah, Saudi Arabia, 2007.
16. Lashin, A.; Al Arifi, N. Geothermal energy potential of southwestern of Saudi Arabia "exploration and possible power generation": A case study at AlKhouba area–Jizan. *Renew. Sustain. Energy Rev.* **2014**, *30*, 771–789. [CrossRef]
17. Lashin, A.; Al Arifi, N.; Chandrasekharam, D.; Al Bassam, A.; Rehman, S.; Pipan, M. Geothermal Energy Resources of Saudi Arabia: Country Update. In Proceedings of the World Geothermal Congress 2015, Melbourne, Australia, 19–25 April 2015.
18. Hussein, M.T.; Lashin, A.; Al Bassam, A.; Al-Arifi, N.; Al Zahrani, I. Geothermal power potential at the western coastal part of Saudi Arabia. *Renew. Sustain. Energy Rev.* **2013**, *26*, 668–684. [CrossRef]
19. Lashin, A.; Al Arifi, N. The geothermal potential of Jizan area, Southwestern parts of Saudi Arabia. *Int. J. Phys. Sci.* **2012**, *4*, 664–675.
20. Berthier, F.; Demange, J.; Iundt, F. *Geothermal Resources of Harrat Khaybar and Harrat Rahat Progress Report 1400-1401 the Kingdom of Saudi Arabia*; Saudi Arabian Deputy Ministry for Mineral Resources Open-File Report BRGM-OF-02-44; Ministry of Petroleum and Mineral Resources: Jiddah, Saudi Arabia, 1982; p. 116.
21. Zahran, H.; Stewart, I.C.F.; Johnson, P.R.; Basahel, M.H. Aeromagnetic-anomaly maps of central and western Saudi Arabia. In *Saudi Geological Survey Open-File Report SGS-OF-2002-8*; 4 Plates; 2003; p. 6.
22. Al-Douri, Y.; Waheeb, S.; Johan, M.R. Exploiting of geothermal energy reserve and potential in Saudi Arabia: A case study at Ain Al Harrah. *Energy Rep.* **2019**, *5*, 632–638. [CrossRef]
23. Civilini, F.; Mooney, W.D.; Savage, M.K.; Townend, J.; Zahran, H. Crustal imaging of northern Harrat Rahat, Saudi Arabia, from ambient noise tomography. *Geophys. J. Int.* **2019**, *219*, 1532–1549. [CrossRef]
24. Abdelwahed, M.F.; El-Masry, N.; Moufti, M.R.; Kenedi, C.L.; Zhao, D.; Zahran, H.; Shawali, J. Imaging of magma intrusions beneath Harrat Al-Madinah in Saudi Arabia. *J. Southeast Asian Earth Sci.* **2016**, *120*, 17–28. [CrossRef]
25. Aboud, E.; Wameyo, P.; Alqahtani, F.; Moufti, M. Imaging subsurface northern Rahat Volcanic Field, Madinah city, Saudi Arabia, using Magnetotelluric study. *J. Appl. Geophys.* **2018**, *159*, 564–572. [CrossRef]

26. Murcia, H.; Németh, K.; Moufti, M.R.; Lindsay, J.M.; El-Masry, N.; Cronin, S.; Qaddah, A.; Smith, I.E.M. Late Holocene lava flow morphotypes of northern Harrat Rahat, Kingdom of Saudi Arabia: Implications for the description of continental lava fields. *J. Southeast Asian Earth Sci.* **2013**, *84*, 131–145. [CrossRef]
27. Langenheim, V.E.; Ritzinger, B.T.; Zahran, H.; Shareef, A.; Al-Dahri, M. Crustal structure of the northern Harrat Rahat volcanic field (Saudi Arabia) from gravity and aeromagnetic data. *Tectonophysics* **2018**, *750*, 9–21. [CrossRef]
28. Aboud, E.; El-Masry, N.; Qaddah, A.; Alqahtani, F.; Moufti, M.R.H. Magnetic and gravity data analysis of Rahat volcanic field, El-Madinah city, Saudi Arabia. *NRIAG J. Astron. Geophys.* **2015**, *4*, 154–162. [CrossRef]
29. Blank, H.R.; Sadek, H.S. *Spectral Analysis of the 1976 Aeromagnetic Survey of Harrat Rahat, Kingdom of Saudi Arabia*; Saudi Arabian Deputy Ministry for Mineral Resources Open-File Report USGS-OF-03-67; Ministry of Petroleum and Mineral Resources: Jiddah, Saudi Arabia, 1983; p. 29.
30. Roy, A.; Dubey, C.P.; Prasad, M. Gravity inversion of basement relief using Particle Swarm Optimization by automated parameter selection of Fourier coefficients. *Comput. Geosci.* **2021**, *156*, 104875. [CrossRef]
31. Singh, K.K.; Singh, U.K. Application of particle swarm optimization for gravity inversion of 2.5-D sedimentary basins using variable density contrast. *Geosci. Instrum. Methods Data Syst.* **2017**, *6*, 193–198. [CrossRef]
32. Rama Rao, B.S.; Murthy, I.V.R. *Gravity and Magnetic Methods of Prospecting*; Arnold-Heinemann: New Delhi, India, 1978.
33. Won, I.J.; Bevis, M. Computing the gravitational and magnetic anomalies due to a polygon: Algorithms and Fortran subroutines. *Geophysics* **1987**, *52*, 232–238. [CrossRef]
34. Rao, C.V.; Pramanik, A.G.; Kumar, G.V.R.K.; Raju, M.L. Gravity interpretation of sedimentary basins with hyperbolic density contrast. *Geophys. Prospect.* **1994**, *42*, 825–839. [CrossRef]
35. Murthy, I.V.R.; Rao, S.J. A FORTRAN 77 program for inverting gravity anomalies of two-dimensional basement structures. *Comput. Geosci.* **1989**, *15*, 1149–1156. [CrossRef]
36. Litinsky, V.A. Concept of effective density: Key to gravity depth determinations for sedimentary basins. *Geophysics* **1989**, *54*, 1474–1482. [CrossRef]
37. Barbosa, V.C.F.; Silva, J.B.C.; Medeiros, W.E. Stable inversion of gravity anomalies of sedimentary basins with non smooth basement reliefs and arbitrary density contrast variations. *Geophysics* **1999**, *64*, 754–764. [CrossRef]
38. Annecchione, M.A.; Chouteau, M.; Keating, P. Gravity interpretation of bedrock topography: The case of the Oak Ridges Moraine, southern Ontario, Canada. *J. Appl. Geophys.* **2001**, *47*, 63–81. [CrossRef]
39. Ekinci, Y.L.; Balkaya, C.; Göktürkler, G.; Özyalın, S. Gravity data inversion for the basement relief delineation through global optimization: A case study from the Aegean Graben System, western Anatolia, Turkey. *Geophys. J. Int.* **2020**, *224*, 923–944. [CrossRef]
40. Silva, J.B.C.; Santos, D.F.; Gomes, K.P. Fast gravity inversion of basement relief. *Geophysics* **2014**, *79*, G79–G91. [CrossRef]
41. Chakravarthi, V.; Shankar, G.B.K.; Muralidharan, D.; Harinarayana, T.; Sundararajan, N. An integrated geophysical approach for imaging subbasalt sedimentary basins: Case study of Jam River Basin, India. *Geophysics* **2007**, *72*, B141–B147. [CrossRef]
42. Qin, P.; Huang, D.; Yuan, Y.; Geng, M.; Liu, J. Integrated gravity and gravity gradient 3D inversion using the non-linear conjugate gradient. *J. Appl. Geophys.* **2016**, *126*, 52–73. [CrossRef]
43. Feng, X.; Wang, W.; Yuan, B. 3D gravity inversion of basement relief for a rift basin based on combined multinorm and normalized vertical derivative of the total horizontal derivative techniques. *Geophysics* **2018**, *83*, G107–G118. [CrossRef]
44. Montesinos, F.G.; Arnoso, J.; Vieira, R. Using a genetic algorithm for 3-D inversion of gravity data in Fuerteventura (Canary Islands). *Geol. Rundsch.* **2005**, *94*, 301–316. [CrossRef]
45. Biswas, A. Interpretation of residual gravity anomaly caused by simple shaped bodies using very fast simulated annealing global optimization. *Geosci. Front.* **2015**, *6*, 875–893. [CrossRef]
46. Toushmalani, R. Gravity inversion of a fault by Particle swarm optimization (PSO). *SpringerPlus* **2013**, *2*, 1–7. [CrossRef]
47. Roy, A.; Kumar, T.S. Gravity inversion of 2D fault having variable density contrast using particle swarm optimization. *Geophys. Prospect.* **2021**, *69*, 1358–1374. [CrossRef]
48. Pallero, J.; Fernández-Martínez, J.; Bonvalot, S.; Fudym, O. Gravity inversion and uncertainty assessment of basement relief via Particle Swarm Optimization. *J. Appl. Geophys.* **2015**, *116*, 180–191. [CrossRef]
49. Pallero, J.L.G.; Fernández-Martínez, J.L.; Fernández-Martínez, Z.; Bonvalot, S.; Gabalda, G.; Nalpas, T. GRAVPSO2D: A Matlab package for 2D gravity inversion in sedimentary basins using the Particle Swarm Optimization algorithm. *Comput. Geosci.* **2021**, *146*, 104653. [CrossRef]
50. Pallero, J.; Fernandez-Martinez, J.L.; Bonvalot, S.; Fudym, O. 3D gravity inversion and uncertainty assessment of basement relief via Particle Swarm Optimization. *J. Appl. Geophys.* **2017**, *139*, 338–350. [CrossRef]
51. Camp, V.E.; Roobol, M.J. The Arabian continental alkali basalt province: Part I. Evolution of Harrat Rahat, Kingdom of Saudi Arabia. *GSA Bull.* **1989**, *101*, 71–95. [CrossRef]
52. Downs, D.T.; Stelten, M.E.; Champion, D.E.; Dietterich, H.R.; Nawab, Z.; Zahran, H.; Hassan, K.; Shawali, J. Volcanic history of the northernmost part of the Harrat Rahat volcanic field, Saudi Arabia. *Geosphere* **2018**, *14*, 1253–1282. [CrossRef]
53. Camp, V.E.; Hooper, P.R.; Roobol, M.J.; White, D.L. The Madinah eruption, Saudi Arabia: Magma mixing and simultaneous extrusion of three basaltic chemical types. *Bull. Volcanol.* **1987**, *49*, 489–508. [CrossRef]

54. Camp, V.E.; Hooper, P.R.; Roobol, M.J.; White, D.L. *The Madinah Historical Eruption: Magma Mixing and Simultaneous Extrusion of Three Basaltic Chemical Types*; Saudi Arabian Directorate General of Mineral Resources, Open File Report DGMR-OF-06-32; Ministry of Petroleum and Mineral Resources: Jiddah, Saudi Arabia, 1989; p. 52.
55. Camp, V.E.; Roobol, M.J. *Geologic Map of the Cenozoic Lava Field of Harrat Rahat, Kingdom of Saudi Arabia*; Saudi Arabian Directorate General of Mineral Resources, Geoscience Map GM-123, scale 1:250,000; Ministry of Petroleum and Mineral Resources: Jiddah, Saudi Arabia, 1991.
56. Moufti, M.R.; El-Difrawy, M.A.M.; Soliman, M.A.W.; El-Moghazi, A.K.M.; Matsah, M.I. *Assessing Volcanic Hazards of a Quaternary Lava Field in the Kingdom of Saudi Arabia*; Final Report ARP-26-79; King Abdulaziz City for Science and Technology (KACST): Riyadh, Saudi Arabia, 2010.
57. Moufti, M.R.; Moghazi, A.M.; Ali, K.A. Geochemistry and Sr–Nd–Pb isotopic composition of the Harrat Al-Madinah Volcanic Field, Saudi Arabia. *Gondwana Res.* **2012**, *21*, 670–689. [CrossRef]
58. Shapiro, N.M.; Campillo, M. Emergence of broadband Rayleigh waves from correlations of the ambient seismic noise. *Geophys. Res. Lett.* **2004**, *31*, L07614. [CrossRef]
59. Bensen, G.D.; Ritzwoller, M.H.; Barmin, M.P.; Levshin, A.L.; Lin, F.-C.; Moschetti, M.P.; Shapiro, N.; Yang, Y. Processing seismic ambient noise data to obtain reliable broad-band surface wave dispersion measurements. *Geophys. J. Int.* **2007**, *169*, 1239–1260. [CrossRef]
60. Brenguier, F.; Shapiro, N.; Campillo, M.; Ferrazzini, V.; Duputel, Z.; Coutant, O.; Nercessian, A. Towards forecasting volcanic eruptions using seismic noise. *Nat. Geosci.* **2008**, *1*, 126–130. [CrossRef]
61. Stankiewicz, J.; Ryberg, T.; Haberland, C.; Natawidjaja, D. Lake Toba volcano magma chamber imaged by ambient seismic noise tomography. *Geophys. Res. Lett.* **2010**, *37*, L17306. [CrossRef]
62. Nagy, D. The gravitational attraction of a right rectangular prism. *Geophysics* **1966**, *31*, 362–371. [CrossRef]
63. Kane, M.F. A comprehensive system of terrain corrections using a digital computer. *Geophysics* **1962**, *27*, 455–462. [CrossRef]
64. Dobrin, M.B.; Savit, C.H. *Introduction to Geophysical Prospecting*, 4th ed.; McGraw-Hill Book Co.: New York, NY, USA, 1988; 867p.
65. Gupta, V.K.; Ramani, N. Some aspects of regional-residual separation of gravity anomalies in a Precambrian terrain. *Geophysics* **1980**, *45*, 1412–1426. [CrossRef]
66. Mickus, K.; Aiken, C.L.V.; Kennedy, W.D. Regional-residual gravity anomaly separation using the minimum-curvature technique. *Geophysics* **1991**, *56*, 279–283. [CrossRef]
67. Guglielmetti, L.; Moscariello, A. On the use of gravity data in delineating geologic features of interest for geothermal exploration in the Geneva Basin (Switzerland): Prospects and limitations. *Swiss J. Geosci.* **2021**, *114*, 1–20. [CrossRef]
68. Elhussein, M. New Inversion Approach for Interpreting Gravity Data Caused by Dipping Faults. *Earth Space Sci.* **2021**, *8*, e2020EA001075. [CrossRef]
69. Ekinci, Y.L.; Balkaya, Ç.; Göktürkler, G.; Turan, S. Model parameter estimations from residual gravity anomalies due to simple-shaped sources using Differential Evolution Algorithm. *J. Appl. Geophys.* **2016**, *129*, 133–147. [CrossRef]
70. Biswas, A.; Sharma, S.P. Interpretation of self-potential anomaly over idealized bodies and analysis of ambiguity using very fast simulated annealing global optimization technique. *Near Surf. Geophys.* **2015**, *13*, 179–195. [CrossRef]
71. Heppner, H.; Grenander, U. Stochastic non-linear model for coordinated bird flocks. In *The Ubiquity of Chaos*; Krasner, S., Ed.; AAAS: Washington, DC, USA, 1990; pp. 233–238.
72. Reynolds, C.W. Flocks, herds and schools: A distributed behavioral model. *ACM SiggraphComput. Graph.* **1987**, *21*, 25–34. [CrossRef]
73. Kennedy, J.; Eberhart, R. Particle Swarm Optimization. In Proceedings of the ICNN'95—International Conference on Neural Networks, Perth, Australia, 27 November–1 December 1995; Volume 4, pp. 1942–1948. [CrossRef]
74. Gao, Y.-L.; An, X.-H.; Liu, J.-M. A particle swarm optimization algorithm with logarithm decreasing inertia weight and chaos mutation. In Proceedings of the 2008 International Conference on Computational Intelligence and Security, Suzhou, China, 13–17 December2008; Volume 1, pp. 61–65.
75. Chai, Y.; Hinze, W.J. Gravity inversion of an interface above which the density contrast varies exponentially with depth. *Geophysics* **1988**, *53*, 837–845. [CrossRef]
76. Cordell, L. Gravity analysis using an exponential density-depth function—San Jacinto Graben, California. *Geophysics* **1973**, *38*, 684–690. [CrossRef]
77. Kaso, A. Computation of the normalized cross-correlation by fast Fourier transform. *PLoS ONE* **2018**, *13*, e0203434. [CrossRef]
78. Perez, R.; Behdinan, K. Particle swarm approach for structural design optimization. *Comput. Struct.* **2007**, *85*, 1579–1588. [CrossRef]
79. Nickabadi, A.; Ebadzadeh, M.M.; Safabakhsh, R. A novel particle swarm optimization algorithm with adaptive inertia weight. *Appl. Soft Comput.* **2011**, *11*, 3658–3670. [CrossRef]
80. Xin, J.; Chen, G.; Hai, Y. A particle swarm optimizer with multi-stage linearly-decreasing inertia weight. In Proceedings of the 2009 International Joint Conference on Computational Sciences and Optimization, Sanya, China, 24–26 April 2009; Volume 1, pp. 505–508.
81. Malik, R.F.; Rahman, T.A.; Hashim, S.Z.M.; Ngah, R. New particle swarm optimizer with sigmoid increasing inertia weight. *Int. J. Comput. Sci. Secur.* **2007**, *1*, 35–44.

82. Thompson, D.T. Euldph: A new technique, for making computer-assisted, depth- estimates, from magnetic data. *Geophysics* **1982**, *47*, 31–37. [CrossRef]
83. Whitehead, N.; Musselman, C. *Montaj Gravity/Magnetic Interpretation: Processing, Analysis, and Visualization System, for 3-D Inversion of Potential Field Data, for Oasis Montaj v6.1*; Geosoft Inc.: Toronto, ON, Canada, 2005.
84. Reid, A.B.; Allsop, J.M.; Grauser, H.; Millet, A.J.; Somerton, I.N. Magnetic interpretation in 3D using Euler Deconvolution. *Geophysics* **1990**, *55*, 80–91. [CrossRef]
85. Abraham, E.M.; Alile, O.M. Modelling Subsurface Geologic Structures at Ikogosi Geothermal Field, Southwestern Nigeria, using Gravity, Magnetics, and Seismic Interferometry Techniques. *J. Geophys. Eng.* **2019**, *16*, 729–741. Available online: https://academic.oup.com/jge/advance-article-bstract/doi/10.1093/jge/gxz034/5531815 (accessed on 3 September 2019). [CrossRef]
86. Rasmussen, R.; Pedersen, L.B. End corrections in potential field modeling. *Geophys. Prospect.* **1979**, *27*, 749–760. [CrossRef]
87. Blaikie, T.N.; Ailleres, L.; Betts, P.G.; Cas, R.A.F. Interpreting subsurface volcanic structures using geologically constrained 3-D gravity inversions: Examples of maar-diatremes, Newer Volcanics Province, southeastern Australia. *J. Geophys. Res. Solid Earth* **2014**, *119*, 3857–3878. [CrossRef]
88. Silva, J.B.C.; Teixeira, W.A.; Barbosa, V.C.F. Gravity data as a tool for landfill study. *Environ. Geol.* **2009**, *57*, 749. [CrossRef]
89. Chen, Z.; Meng, X.; Zhang, S. 3D gravity interface inversion constrained by a few points and its GPU acceleration. *Comput. Geosci.* **2015**, *84*, 20–28. [CrossRef]
90. Pellaton, C. *Geologic Map of the Al Madinah Quadrangle, Sheet 24D*; Kingdom of Saudi Arabia (with Text): Saudi Arabian Directorate General of Mineral Resources Geologic Map GM-52C, Scale 1:250,000; Ministry of Petroleum and Mineral Resources: Jiddah, Saudi Arabia, 1981; 19p.
91. Camp, V.E. *Geologic Map of the Umm Al Birak Quadrangle, Sheet 23D*; Kingdom of Saudi Arabia (with Text): Saudi Arabian Directorate General of Mineral Resources Geologic Map Map GM-87C, Scale 1:250,000; Ministry of Petroleum and Mineral Resources: Jiddah, Saudi Arabia, 1986; 40p.